Modeling Pluto's Minimum Pressure: Implications for Haze Production

Perianne E. Johnson[1a], Leslie A. Young[b], Silvia Protopapa[b], Bernard Schmitt[c], Leila R. Gabasova[c], Briley L. Lewis[d], John A. Stansberry[e], Kathy E. Mandt[f], Oliver L. White[g,h]

[a] *University of Colorado, Boulder, CO, 80303, United States*
[b] *Southwest Research Institute, Boulder, CO, 80302, United States*
[c] *Université Grenoble Alpes, CNES, IPAG, Grenoble Cedex 9, France*
[d] *University of California, Los Angeles, CA, 90095, United States*
[e] *Space Telescope Science Institute, Baltimore, MD, 21218, United States*
[f] *Johns Hopkins University Applied Physics Laboratory, Laurel, MD, 20723, United States*
[g] *NASA Ames Research Center, Moffett Field, CA, 94035, United States*
[h] *SETI Institute, Mountain View, CA, 94043, United States*

Abstract

Pluto has a heterogeneous surface, despite a global haze deposition rate of ~1 μm per orbit (Cheng et al., 2017; Grundy et al., 2018). While there could be spatial variation in the deposition rate, it should coat the surface more uniformly than was observed. One way (among many) to explain this contradiction is for atmospheric pressure at the surface to drop low enough to interrupt haze production and stop the deposition of particles onto part of the surface, driving heterogeneity. If the surface pressure drops to less than 10^{-3} - 10^{-4} μbar and the CH_4 mixing ratio remains nearly constant at the observed 2015 value, the atmosphere becomes transparent to ultraviolet radiation (Young et al. 2018), which would shut off haze production at its source. If the surface pressure falls below 0.06 μbar, the atmosphere ceases

[1] Corresponding author

to be global, and instead is localized over only the warmest part of the surface, restricting the location of deposition (Spencer et al., 1997). In Pluto's current atmosphere, haze monomers collect together into aggregate particles at 0.5 μbar; if the surface pressure falls below this limit, the appearance of particles deposited at different times of year and in different locations could be different. We use VT3D, an energy balance model, to model the surface pressure on Pluto in current and past orbital configurations for four possible static N_2 ice distributions: the observed northern hemisphere distribution with (1) a bare southern hemisphere, (2) a south polar cap, (3) a southern zonal band, and finally (4) a distribution that is bare everywhere except inside the boundary of Sputnik Planitia. By comparing the minima of the modeled pressures to the three haze-disruption pressures, we can determine if or when haze production is disrupted. According to our model, southern N_2 ice is required for haze aggregation to be interrupted, and southern N_2 with very low thermal inertia is required for the possibility of a local or UV-transparent atmosphere.

Keywords: Pluto; Pluto, atmosphere; Pluto, surface; Ices

1. Introduction

The New Horizons mission to Pluto revealed a surprisingly active surface, with dramatic albedo, color, and composition contrasts. The flyby also detected haze in the atmosphere, from which particles should settle through the atmosphere and be deposited onto the surface. These two observations presented a major question: how is the heterogeneity maintained despite a global blanket of deposited haze particles on the surface? This work investigates one possible answer to this question, which is that the atmospheric pressure could drop low enough for long enough over a Pluto orbit to disrupt haze production at its source, preventing the haze particles from being deposited onto the surface.

Pluto's normal reflectance varies across its surface by over a factor of ten, with some regions reaching a normal reflectance value of unity and the darkest regions dropping to a minimum of 0.08 (Buratti et al., 2017). The equatorial region is dark and red, interrupted by bright, more neutral Sputnik Planitia (the expansive volatile-ice sheet that makes up the western half of Tombaugh Regio, Pluto's "heart"; hereafter called SP); midlatitudes, especially where covered by volatile ices, are similar to SP's neutral color, while the north polar region (north of 60°N) has a yellow hue (Stern et al., 2015; Olkin et al., 2017). Composition also varies across the encounter hemisphere, with SP showing very strong N_2 and CH_4 spectral signatures, while the dark equatorial region appears to be free of both species and instead has a spectrum that is consistent with tholins, an unknown mix of hydrocarbons and carbonaceous material produced by cosmic ray and ultraviolet radiation interactions with N_2 and CH_4 (Protopapa et al., 2017; Schmitt et al., 2017).

Deposition rates from Grundy et al. (2018) and Cheng et al. (2017) both predict that a layer of haze particles roughly one micron thick would accumulate over one Pluto orbit, amounting to more than 10 m over the age of the solar system. Cheng et al. (2017) suggest that haze deposition may be interrupted by atmospheric collapse (here, we define collapse to mean when the atmosphere is localized and "patchy" rather than global). Grundy et al. (2018) discuss this possibility as well, and also raise other mechanisms such as a spatially or temporally variable gaseous CH_4 column, or the movement of haze particles by wind once they have settled on the surface, explored further in Bertrand et al. (2019b). Neither paper quantifies the possibility of interrupting or diminishing haze production within the atmosphere.

If the atmospheric pressure at the surface gets low enough, haze production may be altered, suppressed or stopped completely. In Pluto's current atmosphere, haze aggregation occurs at pressures higher than 0.5 μbar, so if the surface pressure drops below this level, monomer haze particles may be deposited instead of aggregates, potentially changing the appearance on the surface (Cheng et al. 2017). We refer to this as a "non-aggregating" atmosphere. For surface pressures less than $\sim$0.06 μbar Pluto cannot support a global atmosphere (Spencer et al. 1997), and instead the atmosphere becomes local, or patchy, which would restrict the region in which haze particles are deposited. Additionally, if the surface pressure drops to less than 10^{-3} - 10^{-4} μbar, the atmosphere would be transparent to ultraviolet radiation (Young et al. 2018). This would shut off the photolysis of atmospheric N_2 and CH_4, suppressing haze production at its source (Gao et al. 2017), while simultaneously boosting the photolysis of surface ices and existing tholins, which can lead to a different composition and appearance of tholins than those produced in the atmosphere (Bertrand et al., 2019a).

Pluto's obliquity varies with a 2.8-million year period, and this obliquity cycle creates extreme seasons during which perihelion occurs simultaneously with northern summer solstice (most recently occurred 0.9 My ago) or aphelion occurs simultaneously with northern summer solstice (most recently occurred 2.4 My ago) (Earle et al., 2017; Bertrand et al., 2018). During these two extreme orbital configurations the minimum surface pressure will be different from that in the current configuration, providing an opportunity for historic haze disruption that might not be seen in today's Pluto. This could affect the present-day surface heterogeneity.

Trafton and Stern (1983) considered a CH_4 atmosphere (CH_4 was then the only species yet detected at Pluto) and predicted a globally-uniform surface pressure for CH_4 column abundances greater than 6.7 cm-Am (using the now-known surface gravity of 0.62 ms^{-2}, this corresponds to a pressure of 0.3 μbar). At the time, the best estimate for the column abundance was 27 ± 7 m-Am (12 ± 3 μbar), which implied that heat could be efficiently transported from high-insolation areas to low-insolation areas, and that vapor pressure equilibrium could maintain a uniform surface temperature of 58 ± 0.9 K. After the discovery of Pluto's atmosphere via occultations in 1988 (Elliot et al., 1989; Hubbard et al., 1988), and the detection of abundant N_2 by Owen et al. (1993), Hansen and Paige (1996) adapted their existing Triton energy balance model to Pluto. They found that volatile transport would be a significant process coupling the surface and atmosphere, allowing surface ices to move around on seasonal timescales. They also found that perennial zonal bands of ice could form in their model, as opposed to perennial polar ice caps, due to Pluto's high obliquity. For some cases, "polar bald spots" were created by sublimation that began at the center of a polar cap rather than at the equatorward edge. N_2 ice temperatures between 30 and 40 K were predicted, based on the balance between insolation, infrared thermal emission, conduction to and from the subsurface, and the latent heat of subliming and condensing N_2.

Bertrand and Forget (2016) used a simplified Pluto GCM to simulate Pluto's climate and volatile transport for thousands of orbits in a reasonable computation time. They found that, for an initial globally uniform distribution of N_2 ice and thermal inertias above 700 tiu (Thermal Inertia Units, J m^{-2} K^{-1} $s^{-1/2}$), all of the N_2 ice migrated into their modeled 3-km deep SP basin within 10,000 Earth years. This motivated the "strawman" example we present in Section 3.2 using a SP-only N_2 distribution. For lower thermal inertias, their model had seasonal deposits of N_2 ice outside of SP. In the higher thermal inertia cases, their model predicted pressures that were consistent with pre-existing occultation measurements (implying a roughly two- to three-fold increase in pressure between 1988 and 2015), as well as a peak value of about 11.5 μbar near 2015. Bertrand et al. (2018) explored the N_2 cycles using their parameterized Pluto GCM on million year timescales, capturing the response to the obliquity cycles described above. They find that a net value of 1 km of N_2 ice has sublimed from the northern edge of SP and recondensed onto the southern edge over the past 2 million years, driven by the change in subsolar latitude at perihelion, which shifted from the southern hemisphere to the north (and is now moving back towards the south, currently near 0°, see Figure 1 in Earle et al. (2017)). They also found that over millions of years the surface pressure on Pluto never drops below tens of nanobars, nor exceeds tens of microbars.

We aim to test the hypothesis of haze disruption via thermal modelling of the surface. Our model, VT3D, is described in Section 2, along with our choices for thermal parameters and the distribution of surface volatiles. Sections 3 presents the resulting pressure evolution curves for the current

Pluto orbit and past orbits with different obliquities and subsolar latitudes at perihelion, assuming four different N_2 distributions. Finally, we discuss the implications of these modelled pressure curves in relation to haze production in Section 4.

2. Methods

2.1. VT3D Model Overview

This section provides an overview of the Volatile Transport Three Dimensional (VT3D) model as used in this study; for a complete description of the model and its full capabilities, see Young (2017). VT3D is an energy balance model, including thermal conduction into and within a substrate, internal heat (not used here), latent heat of sublimation, insolation, and thermal emission. Locally, the energy balance equation is:

$$\frac{S_{1AU}(1-A)\mu}{r^2} - \epsilon\sigma T^4 - k\frac{dT}{dz} + L\dot{m} = 0 \tag{1}$$

where S_{1AU} is the solar constant (1361 W/m^2), A is the Bond albedo of the surface, μ is the solar incidence angle at the given location, r is the heliocentric distance in AU, ϵ is the emissivity of the surface, T is the volatile temperature, k is the heat conductivity, L is the latent heat of sublimation, and $\dot{m}$ is the condensation rate. The partition between sublimation and conduction is determined by global mass balance (Young, 2012, 2013), since the rate of change of the total atmospheric bulk (areal integral of $\dot{m}$) is related to the change in N_2 ice temperature through the change in the surface pressure and atmospheric column density. As implemented here, VT3D depends on three free parameters (the Bond albedo, A, the emissivity, ϵ, and the seasonal thermal inertia, Γ, of the surface N_2 ice) as well as on the spatial distribution of N_2 ice. N_2 is the dominant atmospheric constituent and it is more volatile than the minor constituents of CH_4 and CO, so we consider only the N_2 temperature when we model the atmospheric pressure.

We run VT3D using the explicit form of the equations (rather than its semi-implicit Crank-Nicholson scheme). The explicit scheme is only stable for small timesteps; we calculate the temperature at 500 points per Pluto orbit, corresponding to a timestep of about 0.5 Earth year. The volatiles are discretized vertically into $J = 40$ layers for a total depth of roughly 10 thermal skin depths. The temperature at the next timestep of a given layer depends on the temperature at the current timestep in the layer above, in the layer itself, and in the layer below. To evaluate the insolation term, we average the insolation at the start and end of the current timestep: $(S_n + S_{n+1})/2$, where subscript n represents the current timestep, and *n+1* is the next timestep. To evaluate the thermal emission term, VT3D uses the first-order Taylor expansion of T^4: $\epsilon\sigma T_{0,n}^4 + 2\epsilon\sigma T_{0,n}^3(T_{0,n+1} - T_{0,n})$, where the first subscript indicates the layer (0 corresponds to the top layer) and the second indicates the timestep. The conduction term is discretized using a first-order finite difference scheme; for example the term describing conducted heat from the layer below into the top layer is: $\sqrt{\omega}\Gamma(T_{0,n} - T_{1,n})/\delta$, where ω is the orbital frequency of Pluto, in seconds, and δ is the dimensionless distance between layers. The sublimation rate is related to the rate of change of temperature since we assume vapor pressure equilibrium; in response to an increase in the ice temperature, the vapor pressure above it must also increase, which means particles sublimate from the ice surface, removing latent heat. Thus, the sublimation term is written: $\Phi^A(T_{0,n+1} - T_{0,n})$, where Φ^A is given by: $\Phi^A = L^2 mp\omega/(f_v gkT_{0,n}^2 \tau)$ (L is the latent heat of sublimation for N_2, m is the molecular mass of N_2, p is the vapor pressure at temperature $T_{0,n}$, f_v is the fraction of the surface covered by N_2, g is the surface gravity, k_B is the Boltzmann constant, and τ is a dimensionless time step). After inserting these terms into Equation 1, temperatures at the next timestep are a function of temperatures at the current timestep and various parameters of the N_2 ice. VT3D finds the temperatures by stepping forward in time for one Pluto orbit.

VT3D begins with an analytic approximation to the solution, which is used as the initial guess in the more accurate numerical solution to decrease convergence time. A description on how to implement the analytic solution for quick calculation is included in the Appendix.

To convert temperatures into pressures, we use the equation for solid N_2 vapor pressure as a function of temperature presented in Fray and Schmitt (2009):

$$ln\left(P_{sub}\right) = A_0 + \sum_{i=1}^{n} \frac{A_i}{T^i} \tag{2}$$

Fray and Schmitt (2009) compile previously-published empirical relations and experimental data to find the best-fit coefficients A_i for solid N_2 ice, with separate sets of coefficients for the α- and β-crystalline phases, shown in Table 1.

2.2. Volatile Distribution

Observations of the surface volatile distribution were performed by the LEISA infrared spectrometer on the New Horizons spacecraft. N_2 is detectable by a weak 2.15 μm spectral feature, but only for sufficiently large

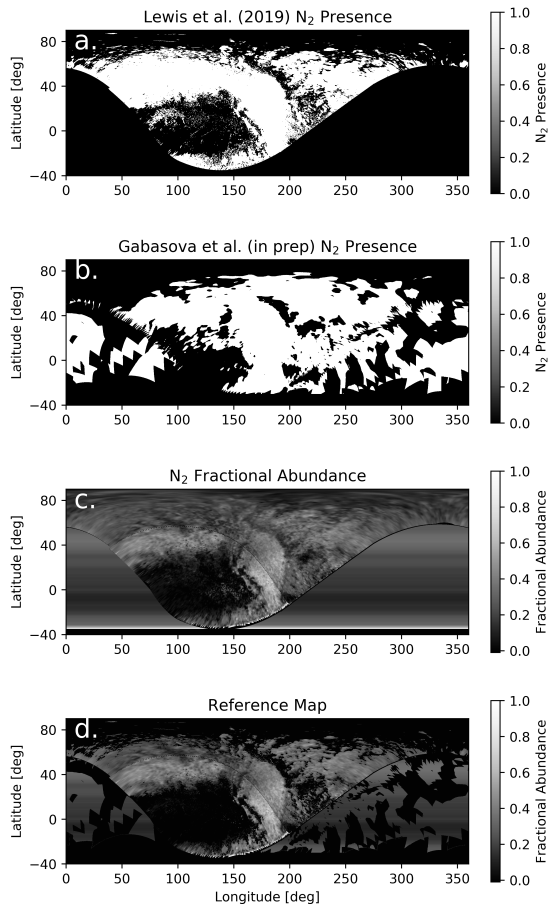

Figure 1: In all panels, white indicates the presence of N_2 ice and black indicates bare areas. Gray indicates the fractional abundance of N_2 in that region. (a) Lewis et al. (2019) N_2 presence map (encounter hemisphere only) which combines the band depth map from Schmitt et al. (2017) and the fractional abundance map from Protopapa et al. (2017). Assumes a band depth greater than 0.005 or a fractional abundance of greater than 0% indicates presence of N_2. (b) Gabasova et al. (in prep) N_2 presence map created from lower-resolution approach band depth data in combination with the higher resolution flyby data. Assumes a band depth greater than 0.005 indicates presence of N_2. (c) Fractional abundance of N_2 from Protopapa et al. (2017) on the encounter hemisphere, and a zonal average fractional abundance on the non-encounter hemisphere. (d) The N_2 distribution used for the northern hemisphere throughout this work, referred to as the reference map.

	A_0	A_1	A_2	A_3	A_4	A_5
α-phase	12.404174	-807.35728	-3925.5143	62965.429	-463269.99	1.324999.3
β-phase	8.51384232	-458.386541	-19871.6407	480001.675	-4523786.13	0

Table 1: Coefficients needed to calculate the equilibrium vapor pressure as a function of temperature, for both $\alpha-$ and β-phase N_2, using Equation 2. These are higher precision values than those presented in Table 5 of Fray and Schmitt (2009).

grain sizes. Its presence can also be inferred from a wavelength shift in CH_4 spectral bands that occur when CH_4 is dissolved in N_2, and from the overall infrared brightness (Protopapa et al., 2017; Schmitt et al., 2017). Protopapa et al. (2017) use a combination of these features along with Hapke radiative transfer modeling to produce a map of N_2 on the encounter hemisphere. Other analyses relying on spectral parameters like band depth or equivalent width are not able to distinguish between relative abundance changes and grain size changes across the surface. Protopapa et al. (2017) produce separate fractional abundance and grain size maps. The modeled grain sizes (where grain size refers to distance between scattering centers, see Hapke (1993)) range from a few centimeters to larger than 1 meter. The fractional abundance map highlights the large, flat ice sheet of SP, along with a latitudinal band stretching from 35°N to 55°N, as the main N_2 reservoirs on the surface, containing up to about 60% N_2 (assuming an areal mixture with other species). Schmitt et al. (2017) present a spatial distribution map of the N_2 ice band depth, as well as a map of the presence of the N_2-rich phase (called the 'CH4 band position index' map) and their correlation, which make use of principal component analysis to reduce the noise and remove some instrument artifacts in the spectro-images of the high resolution LEISA data. Lewis et al. (2019) created a N_2 presence map which combines the band depth map from Schmitt et al. (2017) and the fractional abundance map from Protopapa et al. (2017). This map, shown in Figure 1a, assumes a band depth above 0.005 or a fractional abundance of greater than 0% indicates the presence of N_2. In all panels of Figure 1 white indicates the presence of N_2 ice, black indicates bare areas, and grayscale indicates the fractional abundance. In reality, the N_2-covered areas have varying thicknesses of ice, with SP having perhaps 5 km of ice (McKinnon et al., 2016) while the midlatitude deposits may be much thinner.

The high resolution LEISA images are limited to the encounter hemisphere, which was visible to the spacecraft during the flyby. The widest extent is near SP at longitudes around 150°, where the high resolution coverage reaches from north pole to 30°S. The region tapers off to the east and west until it reach the permanently lit north polar region extending out to 60°N. Most of the southern hemisphere (south of 40°S) is currently in polar night.

Gabasova et al. (in prep) have used lower-resolution approach data in combination with the higher resolution flyby data to create a global N_2 distribution map that includes both the non-encounter and encounter hemispheres, shown in Figure 1b. This map shows the spatial distribution of the 2.15 μm N_2 band depth alone, and does not consider the shifting of the CH_4 bands nor the overall brightness of the pixel. A band depth value of 0.005 or greater indicates the presence of N_2 ice; however since band depth does not directly relate to the fractional abundance of N_2, this cannot be directly converted into a fractional abundance map. Attempts to correlate band depth and fractional abundance using the overlapping encounter hemisphere data did not yield a clear relationship, due in part to the grain size dependence of band depth. Instead, we turn the band depth map from Gabasova et al. (in prep) into a N_2 presence map by applying a band depth threshold of 0.005, analogous to the procedure used by Lewis et al. (2019). We then find the zonal-average fractional abundance in each latitude band, defined by a row of pixels, from the Protopapa et al. (2017) N_2 map (excluding pixels that fall within SP), and assign every pixel on the non-encounter hemisphere in that row this mean value. This fractional abundance map is shown in Figure 1c. The final map combines Figures 1a, 1b, and 1c: on the encounter hemisphere, we assume the product of the Lewis et al. (2019) N_2 presence map and the fractional abundance map from Figure 1c, while on the non-encounter hemisphere we assume the product of the Gabasova et al. (in prep) N_2 presence map and the fractional abundance map from Figure 1c. Hereafter referred to as the reference map, our assumed N_2 spatial distribution map for latitude north of 35°S is shown in Figure 1d.

Our base distribution is always the reference map, but we make different assumptions for the unobserved southern hemisphere (south of 35°S). We use (i) a bare southern hemisphere, (ii) a south polar cap, and (iii) a southern zonal band of N_2 ice. We also present results from a simplified case assuming SP contains the only surface deposit of N_2, to emphasize the significant effect of this feature on the global pressure.

For each choice of N_2 distribution, we calculate the spatially-averaged insolation onto the surface ices as a function of time, which is an input to

VT3D, as shown in Figure 2. In doing so, we assume that the distributions are static in time, and that the surface ices are in vapor pressure equilibrium with the atmosphere, and can thus be described by a single temperature dependent on the average insolation. Assuming a static distribution is a simplification, which allows us to investigate multiple distributions at a lower computational cost, but it is also motivated by the fact that many of Pluto's N_2 ice deposits appear to be perennial (persisting for longer than one orbit). SP is a perennial feature: the surface of the ice sheet is estimated to be less than 10 My old (White et al., 2017) based on the lack of impact craters, but the ice sheet is undergoing convection with an overturning timescale of 0.5 My which cyclically refreshes the surface, allowing the ice sheet to be much older than the crater-derived age. The underlying basin is ancient and likely greater than 4 Gy old (Moore et al., 2016). Numerical simulations from Bertrand and Forget (2016) found that all of the N_2 ice was sequestered into a 3-km deep SP-like basin within 10,000 Earth years, where it stayed for the remainder of the 50,000-year simulation, strengthening the already-strong argument for a perennial SP. It is not as obvious if the other N_2 deposits in the reference map are perennial and last for many Pluto years, or only seasonal and disappear due to sublimation on timescales of tens of Earth years. N_2 is observed at lower altitudes in the northern mid-latitudes (e.g., Howard et al. (2017)) in depression floors that appear flat and smooth. This suggests a deeper, perennial N_2 deposit, coating and smoothing underlying rough terrain, rather than an seasonal deposit of a few meters or less. Bertrand et al. (2019a) showed that the mid-latitude N_2 deposits in the northern hemisphere tend to be seasonal, especially those located within depressions. It is unknown

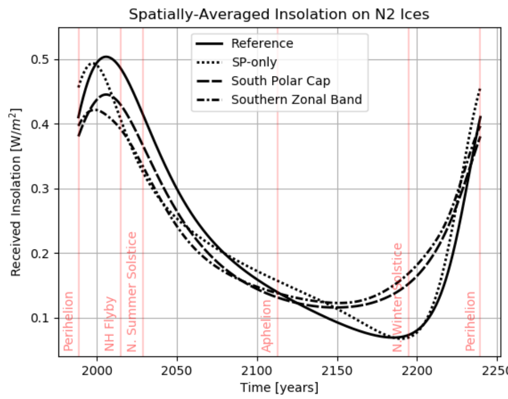

Figure 2: Spatially-averaged insolation onto the N_2 ice in each of our four distributions: reference model (solid line), SP-only model (dotted), south polar cap model (dashed), and southern zonal band (dash-dotted). The x-axis shows time in Earth years spanning one Pluto orbit, beginning in 1988.

whether N_2 exists at mid to high southern latitudes, and, if it does, whether it is perennial or seasonal. For computational expediency, we investigate only static southern distributions too. Here, the term "static" refers only to the locations of the N_2 ice; N_2 still sublimes from areas of high insolation and condenses onto areas of low insolation, but initially bare locations and initially N_2 ice-covered locations remain so throughout the length of our models. Future work could relax the requirement of a static distribution and time-constant physical parameters, in order to study various feedback effects, such as condensation of N_2 onto winter latitudes (Hansen et al., 2015; Bertrand et al., 2018); runaway albedo feedbacks (Earle et al., 2018); or the impact of haze on the albedo, emissivity, or thermal inertia.

2.3. Parameter Space Search

For each choice of N_2 distribution, we explore three free parameters: the Bond albedo, A, the emissivity, ϵ, and the thermal inertia, Γ, of the surface N_2 ice. We assume for simplicity that each of these parameters is uniform across all of the N_2 ice and constant in time. We perform a grid search of albedo and thermal inertia values, and use the emissivity value that is required to match the New Horizons radio occultation surface pressure of 11.5±0.7 μbar in 2015 (Hinson et al., 2017). To do so, we start with an initial guess at the emissivity, calculate the 2015 surface pressure, and then use a Newton-Raphson solver to iteratively find the emissivity value which returns the closest pressure to 11.5 μbar. We explore the full range of Bond albedos (between 0 and 1), and thermal inertias between 25 and 2000 tiu ($Jm^{-2}K^{-1}s^{-1/2}$). Lellouch et al. (2013) calculates diurnal thermal inertias based on TNO observations on the order of 10 tiu, much lower than the annual values we derive for most cases (by "diurnal thermal inertia", we mean thermal inertia of the material within the diurnal skin depth, while "annual skin depth" corresponds to the material within the annual or seasonal skin depth). Spencer and Moore (1992) report thermal inertia values for pure N_2 between 530 and 590 tiu, whether the N_2 is in the α- or β-crystalline phase. On Pluto, the N_2 ices are mixed with some CH_4 and CO, lay above an H_2O ice substrate ($\Gamma = 2100$ to 2200 tiu, as reported for Triton in Spencer and Moore (1992)), and could be "fluffy", fractured, or otherwise distinct from a pure lab sample of ice. Thus, we explore a wide range of thermal inertia values in this model. For each A, Γ, ϵ triplet we calculate a surface pressure versus time curve using 500 timesteps per orbit. To ensure convergence, we initialize the numerical

VT3D model using the analytic approximation as our initial guess, and we run the model over 20 orbits before selecting the final orbit as our result. Details of the analytic approximation are given in the appendix.

Once we have a grid of pressure curves (one for each A, Γ, ϵ triplet), we apply two constraints to eliminate some regions of this parameter space. The first is to eliminate any cases where the emissivity required to match the 2015 New Horizons pressure is outside of the range $0.3 < \epsilon < 1$. An emissivity greater than unity is unphysical, and we impose a lower bound of 0.3. Stansberry et al. (1996) use Hapke theory to calculate N_2 emissivity as a function of grain size and temperature, and found that the emissivity remains above 0.3 at temperatures between 20 and 60 K for grains larger than 1 cm (nearly all grains on Pluto are centimeter-sized or larger, as derived by Protopapa et al. (2017)). The second constraint is observational. From the record of stellar occultations going back to 1988, Pluto's atmospheric pressure as sensed by occultations roughly doubled or tripled between the discovery of its atmosphere in 1988 and the New Horizons flyby in 2015. Occultations do not reach all the way to the surface, so we cannot say for certain whether or not the surface pressure experienced the same two- to three-fold increase. If we assume that the surface pressure increase during this time period was the same as the 1205-km altitude pressure increase, then we find $3.14 > P_{2015}/P_{1988} > 1.82$ at the 3-σ level for the surface pressures (Elliot et al., 2003; Hinson et al., 2017). We eliminate any (A,Γ,ϵ) triplets where the ratio of our modeled 2015 and 1988 surface pressures is outside of this range.

3. Results

The dependence of the shape and amplitude of the pressure curve on each of the three parameters is explored in Figure 3. The leftmost panel holds the thermal inertia and emissivity constant, at 1000 tiu and 0.7, respectively. For a higher albedo, the resulting pressure is lower at every point in time, due to the lower input of solar energy. The middle panel shows the dependence of pressure on emissivity, while holding albedo constant at 0.7 and thermal inertia at 1000 tiu. The dependence is similar to that of albedo; as emissivity increases the pressure curve is lower at every timestep, as the heat is re-radiated away from the surface more efficiently. The rightmost panel shows how the pressure curve depends on thermal inertia, while albedo and emissivity are both constant at 0.7. A lower thermal inertia surface will experience a larger range of pressures over an orbit compared to a higher thermal inertia one, since the lower thermal inertia surface responds more quickly to changes in the input energy. High thermal inertia materials conduct heat towards the surface more efficiently and thus compensate more efficiently for any change in thermal balance at the surface (e.g. the cooling of the surface by thermal emission).

In the following sections, we present the annual pressure versus time curves for the wide range of parameter values we explored, for each of our four possible N_2 distributions, and for both Pluto's current orbital configuration and past "superseasonal" configurations. We begin with our reference model, which is the reference map and a bare southern hemisphere. Sections 3.2 through 3.4 present the results from our alternative models, which are (1) a N_2 distribution map where the surface is assumed to be entirely bare except

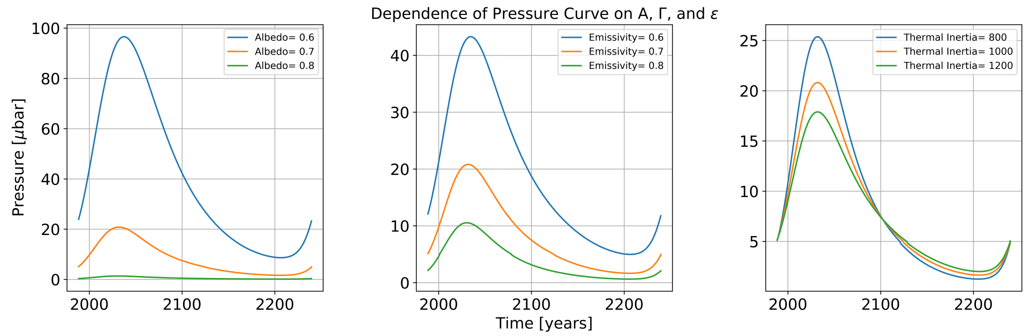

Figure 3: Dependence of the shape of the pressure curve on each of the three free parameters. (Left) Dependence on albedo, for constant thermal inertia of 1000 tiu and emissivity of 0.7. (Center) Dependence on emissivity, for constant albedo of 0.7 and thermal inertia of 1000 tiu. (Right) Dependence on thermal inertia, for constant albedo of 0.7 and emissivity of 0.7.

for the N_2 ice contained in SP, (2) the reference map with a south polar cap, (3) the reference map with a southern zonal band.

3.1. Reference Model

We first present the results from Pluto's current orbit using the reference map, along with a bare southern hemisphere.

After applying the constraints as described above for the reference model pressure curves, the remaining allowed parameter space is shown as the grayscale boxes in Figure 4. Albedos between 0.6 and 0.9 and thermal inertias above 400 tiu satisfy the constraints, with lower albedos requiring higher thermal inertias. All of the cases that had allowable emissivity values and pressure increases between 1988 and 2015 had minimum pressures between 1 and 3 μbar. There are no (A,Γ,ϵ) triplets that drop below the 0.5 μbar haze

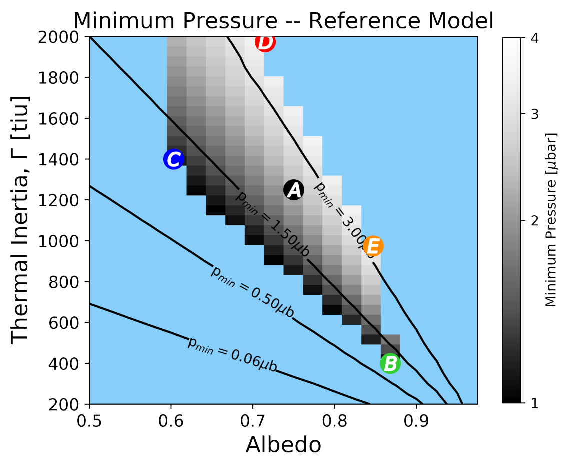

Figure 4: Restricted parameter space for Pluto's current orbit and the reference map (bare southern hemisphere) after choosing ϵ to ensure $P_{2015} = 11.5$ μbar, and applying the two further constraints: (1) $1 > \epsilon > 0.3$ (2) $3.14 > P_{2015}/P_{1988} > 1.82$. Grayscale and black diagonal contour lines show the minimum pressure experienced over a Pluto year for that combination of A and Γ.

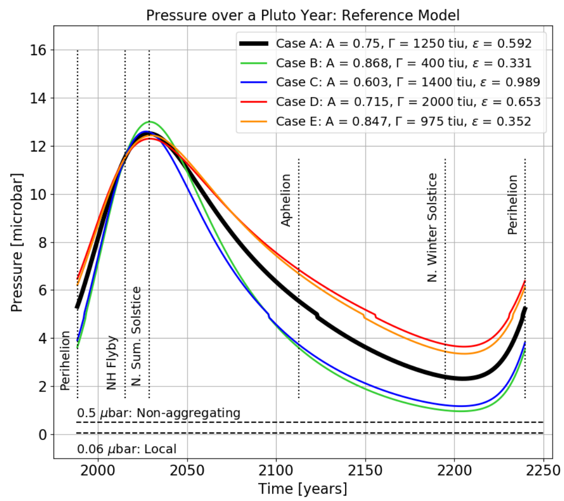

Figure 5: Pressure versus time curves for Pluto's current orbit and the reference map (bare southern hemisphere). The 2% discontinuity at 5 μbar reflects the small difference in the calculated pressure at the α-β transition temperature (see text for details).

aggregation limit or the 0.06 μbar local atmosphere limit, or the even lower atmospheric transparency limit for Pluto's current orbit.

The pressure curves for five example cases are shown in Figure 5. The thick black line (case A) shows a central case with A = 0.75, Γ = 1250 tiu, and $\epsilon = 0.592$. Case A shows an increase in pressure between perihelion and the peak of pressure just after the time of the New Horizons flyby, and then a slow decrease to the minimum pressure near northern winter solstice. The delay between perihelion and the peak of pressure is primarily due to the subsolar latitude dependence. The N_2 ices receive the strongest spatially-averaged insolation near 2008 (see Figure 2), which is determined in part from the $1/r^2$ dependence but more strongly depends on the incidence angle of sunlight onto SP. Thermal inertia adds to this delay as well. The jump

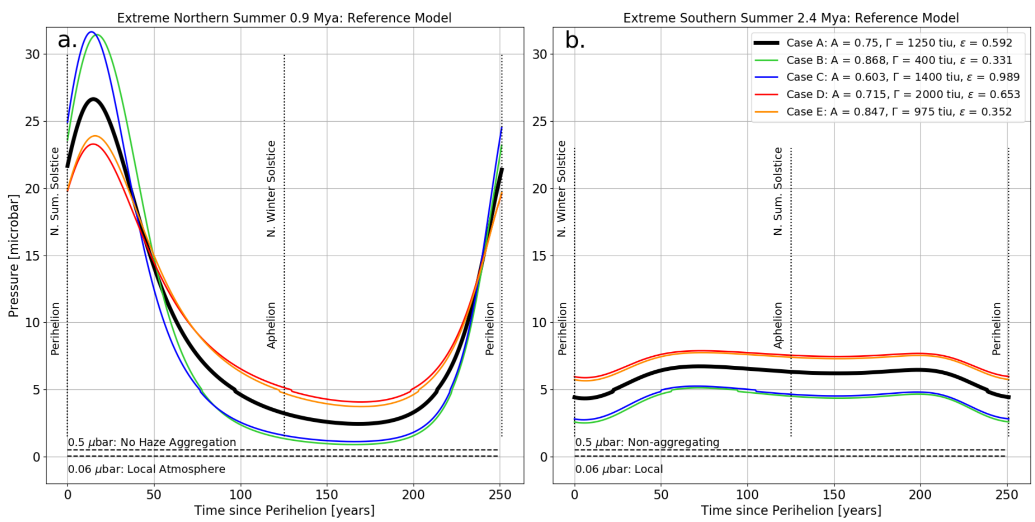

Figure 6: (a) Reference model pressure versus time curves for Pluto's orbit 0.9 Mya, when it was experiencing short, intense northern summers. (b) Reference model pressure versus time curves for Pluto's orbit 2.4 Mya, when it was experiencing long, mild northern summers.

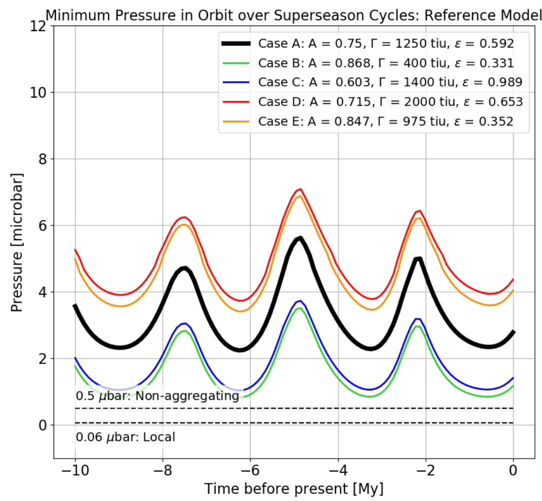

Figure 7: Annual minimum pressure experienced at Pluto's surface over the past 10 My for each of the five test cases, using the reference model.

in pressure near 5 μbar present in all five of the curves is caused by the small numerical discontinuity of 2% at the change in the form of the vapor pressure equation at the α-β transition of N_2, which occurs at 35.6 K (Fray and Schmitt, 2009).

The blue and green curves (cases B and C) are example cases that remain colder (and therefore have a lower surface pressure) than case A throughout most of the orbit. The combination of case B's higher albedo and low thermal inertia compensate for the effect of the low emissivity, keeping the surface colder than in case A. Case C has a lower albedo and a higher emissivity (so it effectively reradiates away the insolation), causing it to be consistently colder. The red and orange curves (cases D and E) in Figure 5 are example cases that remain warmer than case A throughout most of the orbit. Case D has a similar albedo and emissivity as case A, but experiences a smaller range of pressures due to the higher thermal inertia. Case E has a higher albedo than case A and a lower emissivity, so it is able to remain warmer despite a lower thermal inertia by reradiating the input solar insolation less effectively. None of the test cases predict pressures below any of the haze-important pressures; the atmosphere never becomes non-aggregating, local, nor UV-transparent. This reference model predicts a maximum in the pressure between 2027 and 2030, after which the surface pressure will begin to decrease.

As evident in Figure 5, extrema in the surface pressure occur close to solstices, when the primarily-northern N_2 deposits are receiving the most (or least, in the case of winter solstice) direct insolation. If northern summer solstice occurs near perihelion, the N_2 deposits will be receiving the most direct insolation (smallest incidence angle) when they are also receiving the most intense insolation (closest to the Sun), creating a strong but short northern summer. Conversely, if northern summer solstice occurs near aphelion, they will be receiving the most direct insolation (smallest incidence angle) when they are receiving the least intense insolation (farthest from the Sun), creating a mild but long northern summer. In order to investigate Pluto's pressure during these extreme seasons, we used the same five example cases as the current orbit and ran VT3D back 10 My, adjusting the obliquity, eccentricity, and subsolar latitude at perihelion according to Earle et al. (2017). Figure 6 shows the pressure versus time curve for the five example cases using our reference model during a period of intense northern summer 0.9 Mya (panel a) and a period of intense southern summer (and hence mild northern summer) 2.4 Mya (panel b). The color scheme and labelling of the cases remains the same as Figures 4 and 5.

Figure 6a clearly shows the extreme summer characteristic of the orbital configuration Pluto was in 0.9 Mya, with a sharp peak just after perihelion and a wide, low minimum in the pressure curve. The pressure varies wildly over an orbit, ranging between 2.5 and 27 μbar for case A. Despite this wide range, none of the example cases drop below any of the pressures important to haze production, so haze would not be affected during this time period.

During the mild northern summer at 2.4 Mya shown in Figure 6b, the pressure curves are noticeably flatter than the 0.9 Mya configuration and have a long peak-plateau where the pressure is stable. Since the reference model assumes a bare southern hemisphere (south of 35°S), the southern summer is not particularly extreme; at perihelion/southern summer solstice, the spatially-averaged insolation is very low since no N_2 deposits are receiving direct insolation, which causes the pressure to be low as well. In this configuration, like the current orbit and 0.9 Mya, none of the example cases become cold enough to disrupt haze.

Figure 7 shows the minimum pressure experienced over an orbit for the past 10 My (roughly three full obliquity cycles) for the five example cases. None of these curves fall below the 0.5 μbar nor the 0.06 μbar levels, or the even lower atmospheric transparency pressure levels. Depending on the choice of albedo, thermal inertia, and emissivity, this model predicts a minimum pressure over the past 10 My between 1 and 4 μbar.

3.2. Sputnik Planitia-only Model

Next, we discuss the results from our alternative models, beginning with a N_2 distribution in which SP is the only source of N_2 on the surface. Figure 8 shows the N_2 distribution for this alternative model. Both the band depth map (Schmitt et al., 2017) and the Hapke modeling map (Protopapa et al., 2017) clearly indicate deposits of N_2 ice outside of SP, but by limiting this distribution to SP alone, we can investigate the relative influence of SP on the climate compared to the other N_2 deposits. SP is 1000 km in diameter (covering 5% of Pluto's total surface area), estimated to be 4 to 10 km thick, and has a fractional N_2 abundance as high as 60%, meaning that as much as 60% by area of each pixel is covered by N_2 (Protopapa et al., 2017). SP is located near the equator, spanning from 20°S to 50°N, so it remains at least partially illuminated for the full range of subsolar latitudes experienced over an orbit. For these reasons, we expect SP to be a strong driver of the atmospheric pressure, and thus expect the SP-only model results to be very similar to the reference model results. This distribution also allows a more direct comparison with Bertrand and Forget (2016), in which N_2 was sequestered into a circular SP-analog basin very similar to this distribution.

Figure 9 shows the restricted parameter space for the SP-only model. In comparison with Figure 4 for the reference model, lower thermal inertias are required for the SP-only model. Ignoring all of the N_2 ice outside of SP causes the peak in the spatially-averaged insolation to occur sooner after perihelion, and for the difference between the peak value and the perihelion value of the spatially-averaged insolation to be smaller (see Figure 2). As a consequence of these two changes to the insolation, lower thermal inertias are needed to compensate, in order to satisfy the constraint on the modeled increase in pressure between 1988 and 2015.

Five example test cases are shown in Figure 10 for the SP-only case. Note that due to the different constrained parameter space, these 5 cases

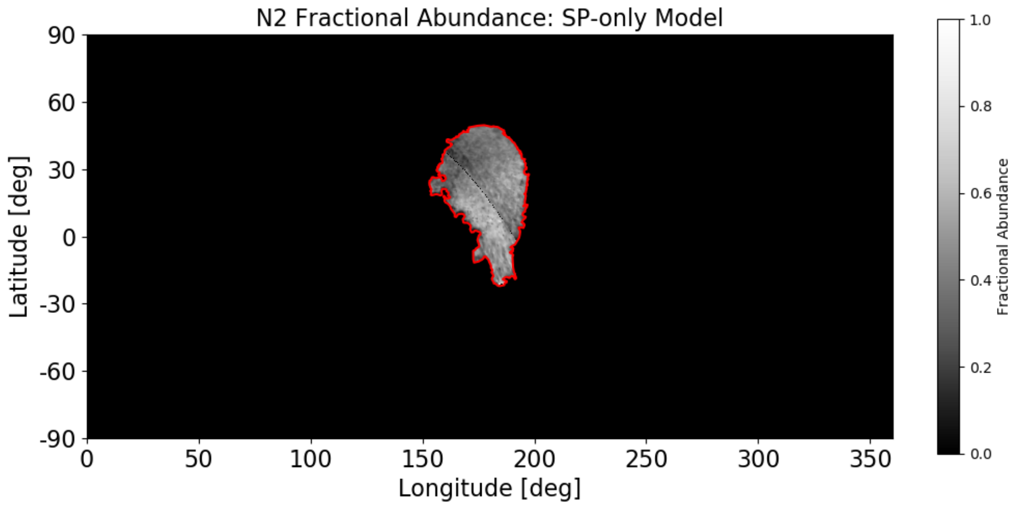

Figure 8: Assumed spatial distribution of N_2 ice for the SP-only model. The red outline shows the boundary of SP as defined by White et al. (2017).

are different than the test cases from the reference model, but the color scheme is the same, with red and orange curves being relatively warmer or higher pressure cases, while the blue and green curves are cooler and therefore lower pressure for much of the orbit. In the SP-only model, the peaks in most of the test case pressures occur slightly earlier, before northern summer solstice, and are slightly lower at 11.5 μbar compared to 12.5 μbar for the reference model test cases. This is again a consequence of the differences in the spatially-averaged insolation between the reference model and the SP-only model. Additionally, the minima in the pressure curves are relatively lower than the reference model case, with the cases B and C dropping below the haze aggregation limit for a period of time near northern winter solstice. This behavior is a consequence of the lower thermal inertias required for

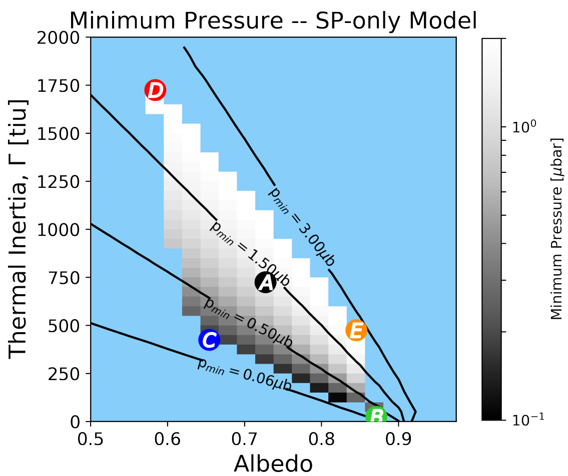

Figure 9: Restricted parameter space for Pluto's current orbit assuming SP is the only N_2 ice deposit, after choosing ϵ to ensure $P_{2015} = 11.5$ μbar, and applying the two further constraints: (1) $1 > \epsilon > 0.3$ (2) $3.14 > P_{2015}/P_{1988} > 1.82$. Grayscale and black diagonal contour lines show the minimum pressure experienced over a Pluto year for that combination of A and Γ.

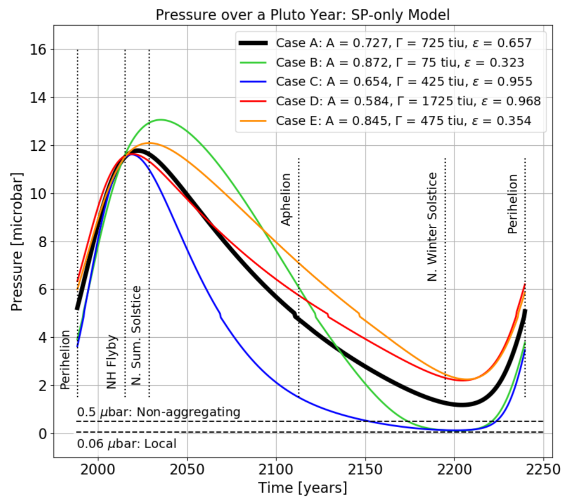

Figure 10: Pressure versus time curves for Pluto's current orbit, assuming SP is the only N_2 ice deposit.

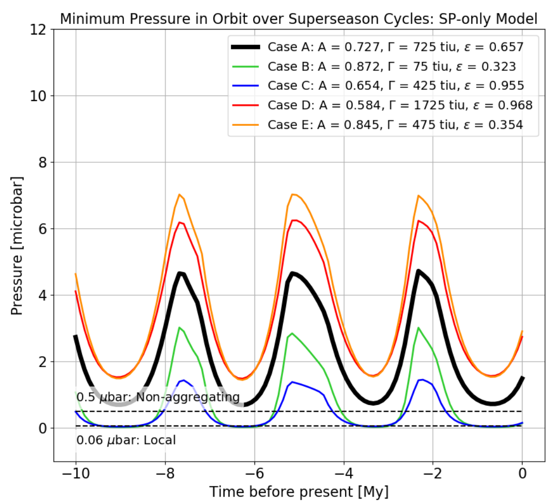

Figure 11: Annual minimum pressure experienced at Pluto's surface over the past 10 My for each of the five test cases, assuming SP is the only N_2 ice deposit.

the SP-only case: lower thermal inertia allows input energy variations to be quickly realized as temperature variations, creating larger temperature and pressure swings. As expected, the general pressure evolution trend is very similar for the SP-only model compared to the reference model, confirming our expectation that SP is a large driver of the seasonal pressure cycle on Pluto.

We investigated the long-timescale behavior of the SP-only model as well. Figure 11 shows the minimum pressure experienced in each orbit going back 10 My, for the same five test cases. Test cases B and C produced some past atmospheres that could have been non-aggregating, but none of the test cases ever predict local atmospheres, meaning the modeled atmospheres never collapse over the past 10 My.

3.3. South Polar Cap Model

Existing models have shown that perennial polar caps are not likely to form on Pluto, due to the high obliquity which causes the poles to receive more annually-averaged insolation than the equator (Young, 2013; Bertrand et al., 2018, 2019a). Prior to the flyby, Young (2013) found that perennial northern volatiles were possible, but that most perennial southern volatile cases could be eliminated based on the modeled pressure increase between 1988 and 2006 not matching the observed increase from occultations. While the simulations of Bertrand et al. (2019a) did not produce perennial polar caps of N_2, many of their simulations (representing a range of thermal inertia and albedo values for the N_2 ice, CH_4 ice, and H_2O substrate) resulted in the formation of a seasonal south polar cap that persisted for 80% to 90% of Pluto's orbit. Observations by New Horizons found the north polar region north of 60°N to be relatively N_2-free, with band depths less than 0.005 and fractional abundances less than 30% (Schmitt et al., 2017; Protopapa et al., 2017). The south polar region was experiencing polar night and was thus unobservable.

Hansen and Paige (1996) found that southern polar caps persist for a greater fraction of the orbit than northern caps, due to the fact that northern summer occurs as Pluto is approaching perihelion (causing rapid sublimation of the north polar cap and subsequent rapid condensation on to the cold southern polar cap), while southern summer occurs when Pluto is approaching aphelion (causing slower sublimation of the southern polar cap and slower condensation onto the northern polar cap). Their model assumed a small N_2 inventory (50 kg/m^2), as did Young (2013), while the global equivalent layer implied by the presence of SP alone (5 km deep, 1000 km in diameter) is on the order of 10^5 kg/m^2. A larger N_2 inventory could mean that polar caps grow thick enough to avoid completely the ice sheetsublimating away during the summer, producing perennial polar caps.

Normal reflectance maps produced from Pluto-Charon mutual events in the late 1980s showed a bright south polar cap (Young and Binzel, 1993). This cap was not necessarily composed of N_2 ice (it could have been bright CH_4 ice as well), but it is evidence that at least seasonal southern caps form on Pluto. Additionally, Grundy and Fink (1996) analyzed 15 years of visible-wavelength spectroscopy (1980-1994) and found that the spectra were consistent with a model in which much of the southern hemisphere (from the pole to 50°S) is covered with a N_2-dominated mix of ices, although other solutions could not be conclusively ruled out.

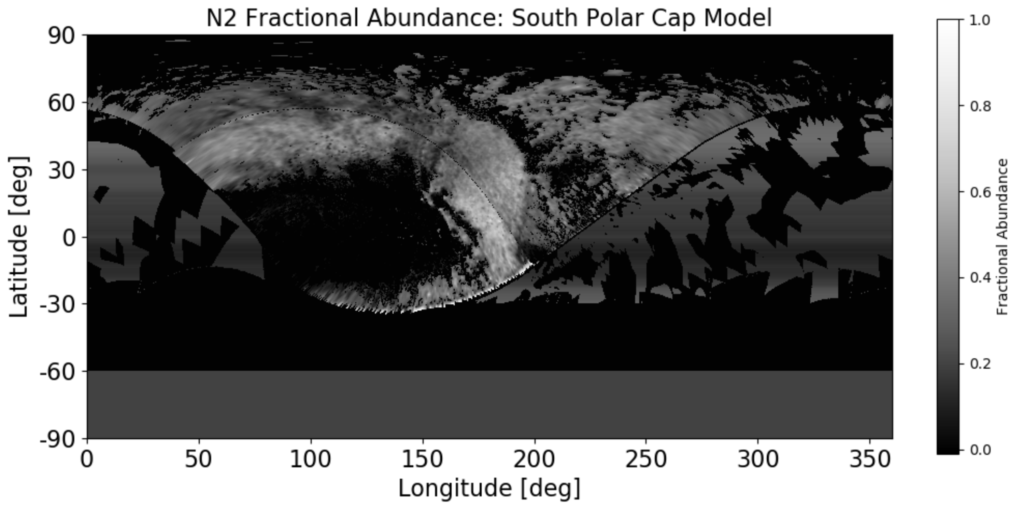

Figure 12: Spatial distribution of N_2 ice for the south polar cap model. Assumes a south polar cap is present extending from the pole to 60°S with a fractional abundance of 20%, in addition to the N_2 present in the reference map.

From the above evidence, we do not rule out the possibility of a perennial south polar cap, or a very long-lasting seasonal south polar cap, and choose to investigate it as one of our alternative models. For our south polar cap, we assume a cap of N_2 ice that extends from the pole to 60°S with a uniform fractional abundance of 20%, as shown in Figure 12. We investigated polar caps with higher fractional abundances, but found that for larger southern deposits of N_2 ice there were no (A,Γ,ϵ) capable of satisfying our constraints.

The region of allowed parameter space for the south polar cap model is shown in Figure 13. Compared the reference model, lower thermal inertias are required, although not as low as the SP-only model. Minimum pressures between 3 μbar and 0.5 μbar are predicted. There are no cases which predict pressures below any of the haze-disruption pressures; aggregation is not in-

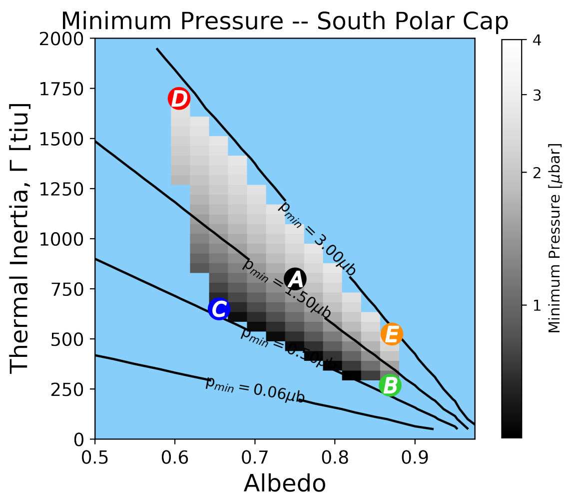

Figure 13: Restricted parameter space for Pluto's current orbit and a south polar cap after choosing ϵ to ensure $P_{2015} = 11.5$ μbar, and applying the two further constraints: (1) $1 > \epsilon > 0.3$ (2) $3.14 > P_{2015}/P_{1988} > 1.82$. Grayscale and black diagonal contour lines show the minimum pressure experienced over a Pluto year for that combination of A and Γ.

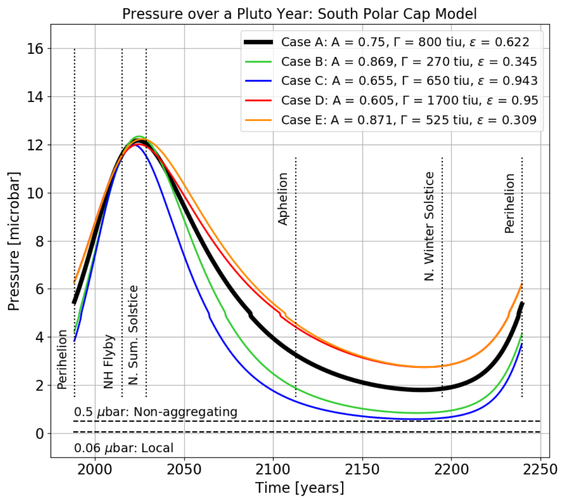

Figure 14: Pressure versus time curves for Pluto's current orbit, for the south polar cap model.

terrupted, the atmosphere remains global, opaque to UV radiation, and does not collapse.

Five test cases from the region of allowed parameter space are shown in Figure 14. Overall, the shape and amplitude of the pressure curves are very similar to those from the reference model, with slightly lower maximum and minimum pressures for the south polar cap model. The pressure falls off more quickly in the south polar cap model, leading to a broader minimum extending from aphelion to winter solstice. This behavior, along with the slightly lower maximum and minimum pressures, occur because the ice in the south polar cap is radiating away energy via thermal emission (as are the northern hemisphere ices), but is obscured in polar night for a large portion of the orbit and thus isn't absorbing any solar insolation.

The superseasonal behavior of the five test cases for the south polar cap

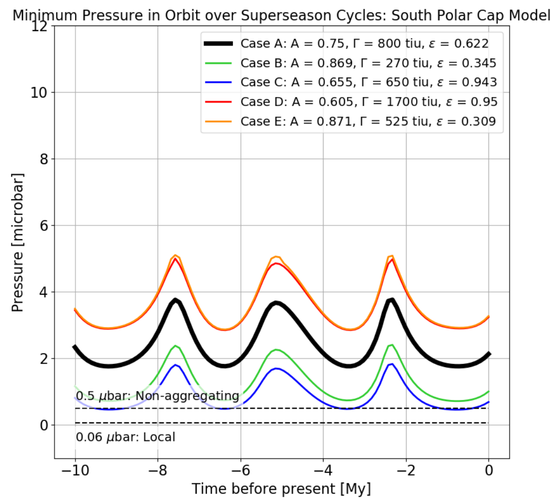

Figure 15: Annual minimum pressure experienced at Pluto's surface over the past 10 My for each of the five test cases, for the south polar cap model.

model is shown in Figure 15. Case C (blue curve) is unique in that the pressure falls below the haze aggregation limit at points in the obliquity cycle despite remaining above the limit in Pluto's current orbital configuration. Near the extreme northern summer period at 0.9 Mya, the minimum pressure over an orbit predicted in Case C drops to 0.47 μbar. In this orbital configuration, the south pole is pointed most directly at the sun at aphelion. The majority of the N_2 ice deposits are not directly illuminated since they are in the northern hemisphere, and despite direct insolation, the N_2 ice at the south pole is not receiving intense insolation due to the high heliocentric distance. Case C has a high emissivity of 0.945, so the unilluminated northern volatiles efficiently reradiate what little solar energy the southern volatiles absorb, causing the low minimum pressure. The other four test cases' combination of albedo, thermal inertia, and emissivity values are able to counteract the orbital configuration's effect on the pressure and their predicted pressures remain above all of the haze-disruption pressures.

3.4. Southern Zonal Band Model

Figure 16 shows the N_2 distribution for the final alternative model we investigate, the southern zonal band model. This distribution consists of the reference map plus a zonal band of N_2 between 35°S and 55°S with a fractional abundance of 20%. This location and fractional abundance was chosen to mirror the northern midlatitude distribution; between 35°N and 55°N there is a band of N_2 with an average fractional abundance of roughly 40%, visible in the reference map and also identified in Protopapa et al. (2017). We initially tried a southern zonal band with a fractional abundance of 40% to match the observed northern band, but found there were no (A,Γ,ϵ) triplets capable of satisfying the constraints we imposed. Having such a significant deposit of N_2 ice in the southern hemisphere produced very high spatially-averaged insolation and therefore high pressures in 1988 (near perihelion and equinox). Even with very low thermal inertias (<50 tiu), it was not possible to double or triple the atmospheric pressure between 1988 and 2015 while requiring that the modeled 2015 pressure be 11.5 μbar. This is consistent with results from Meza et al. (2019), who found that small southern N_2 deposits (or no southern N_2 at all) were required to produce reasonable pressure evolution in which the peak of pressure occurs after 2015. Thus, we adopt a fractional abundance of 20% for the southern zonal band. A northern boundary for this band of 35°S places it just out of view of the high resolution encounter hemisphere images. At the time of the New Horizons flyby in 2015, everything south of 40°S was experiencing polar night.

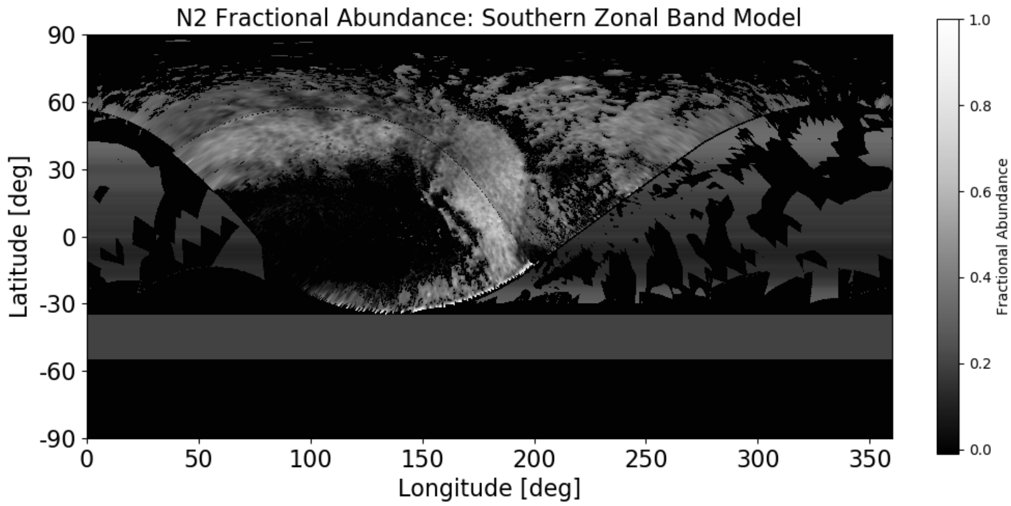

Figure 16: Spatial distribution of N_2 ice for the southern zonal band model. Assumes a zonal band of N_2 is present between 35°S and 55°S with a fractional abundance of 20%, in addition to the N_2 present in the reference map.

Figure 17 shows the region of allowed parameter space for the southern zonal band model. Thermal inertias between 25 and 1000 tiu are able to satisfy our constraints. Minimum pressures range between 1.5 μbar to 0.01 μbar. Many of the (A,Γ,ϵ) triplets produce pressure curves that fall below the haze aggregation limit. Albedos between 0.7 and 0.9 coupled with thermal inertias lower than 200 tiu and nearly the full range of emissivities ($0.3 < \epsilon < 1$) lead to atmospheric collapse.

Five test cases are shown in Figure 18 on a linear scale, and in Figure 19 on a logarithmic scale to highlight the very low pressures near aphelion and northern winter solstice. All of the example cases have perihelion pressures of around 5 μbar, and then the pressure rapidly increases to 11.5 μbar in 2015. Compared to the reference model, the peak in the pressure curve is

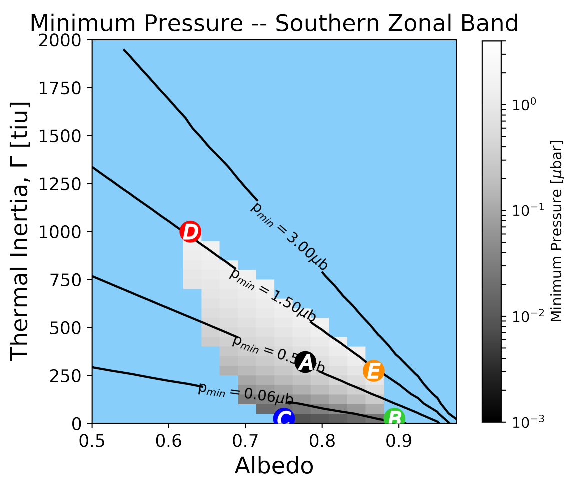

Figure 17: Restricted parameter space for Pluto's current orbit and a southern zonal band after choosing ϵ to ensure $P_{2015} = 11.5$ μbar, and applying the two further constraints: (1) $1 > \epsilon > 0.3$ (2) $3.14 > P_{2015}/P_{1988} > 1.82$. Grayscale and black diagonal contour lines show the minimum pressure experienced over a Pluto year for that combination of A and Γ.

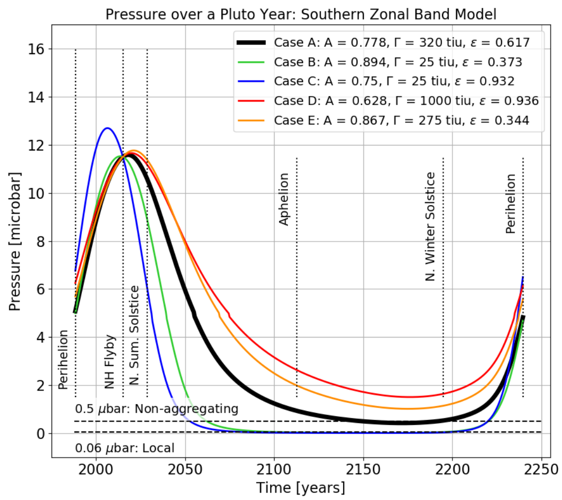

Figure 18: Pressure versus time curves for Pluto's current orbit, for the southern zonal band model (linear scale).

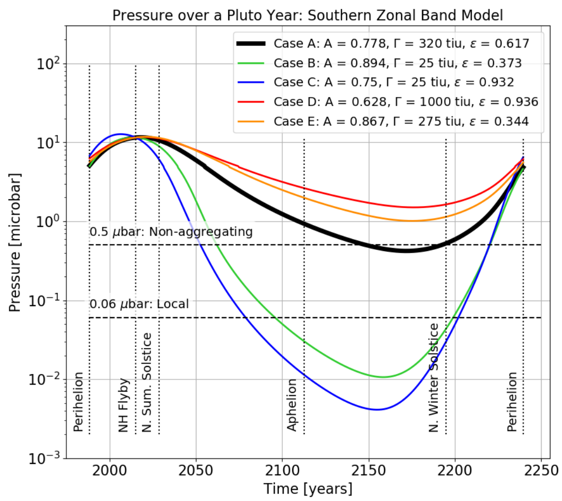

Figure 19: Pressure versus time curves for Pluto's current orbit, for the southern zonal band model (log scale).

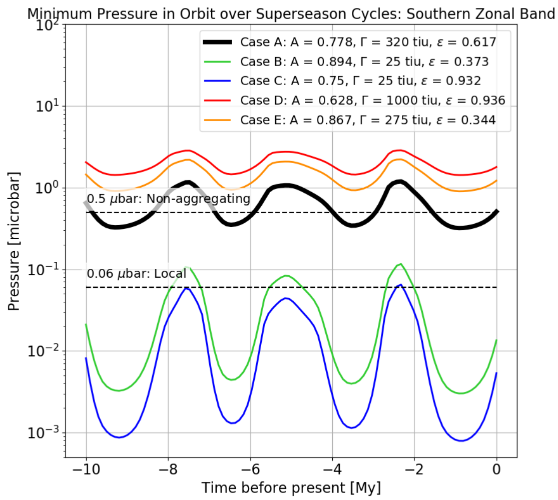

Figure 20: Annual minimum pressure experienced at Pluto's surface over the past 10 My for each of the five test cases, for the southern zonal band model (log scale).

much sharper and the minimum is much broader, due to the lower thermal inertias. The pressure peak occurs earlier in the orbit, around 2015 rather than 2027 for the reference model. This is driven by the spatially-averaged insolation; it is highest near equinox (nearly concurrent with perihelion) when the southern zonal band of N_2 ice and SP are both being directly illuminated, and decreases as the subsolar latitude moves to the north after equinox and the zonal band moves into polar night. The extremely low pressures occur near aphelion and winter solstice, when the spatially-averaged insolation onto the N_2 ices is low, and are due in part to the low thermal inertias which allow for quick temperature and pressure changes.

Figure 20 shows the superseasonal behavior for the five test cases in the southern zonal band model. Three of the five cases predict minimum pressures below the haze aggregation limit. Two of those cases, B (green curve) and C (blue curve), predict a minimum pressure below the local atmospheric limit in nearly every orbit for the past 10 My. All of the test cases produce atmospheres that remain opaque to UV radiation throughout the past 10 My.

4. Haze Implications

In Pluto's current orbit, our reference model fails to produce any case where the pressure drops low enough to interrupt haze. There are no combinations of parameters, namely Bond albedo, thermal inertia, and emissivity, which are simultaneously capable of reproducing the observed 2015 flyby pressure and having a minimum pressure below any of the haze-disruption pressures, in the current orbit. Additionally, on long timescales, there are no cases in our reference model which produce pressures that fall below the haze-disruption pressures. The modeled atmosphere remains haze-aggregating, global, and opaque to UV radiation during the 10 My period we investigated.

Southern N_2 is necessary for haze to be interrupted. Our south polar cap and southern zonal band models both predict that haze aggregation could stop at some point during the orbit, although in the case of our polar cap this is only possible for special orbital configurations when northern summer solstice and perihelion occur at the same time, and then only for low-albedo, low-thermal inertia cases. In the case of the zonal band model, haze aggregation is stopped between aphelion and northern winter solstice in Pluto's current orbit and in many past orbits going back 10 My, for most cases in the allowed parameter space. Stopping haze aggregation for a portion of the orbit could cause the appearance and size of the haze particles being deposited to vary seasonally. The haze was observed globally at the time of the New Horizons flyby, but it was brighter towards the north, probably indicating greater haze mass (Cheng et al., 2017). Deposition rates could be dependent on the brightness, which could vary seasonally. Thus, locations on the surface with a higher deposition rate could be covered with more monomer haze particles than others, explaining the heterogeneity. As demonstrated in Bertrand and Forget (2017), haze production rates as a function of latitude and time can be determined based on the assumed UV flux at the top of Pluto's atmosphere and the opacity of the atmosphere. This same technique could be applied to our results, in order to determine which latitudes would experience the largest decrease in haze production resulting from atmospheric collapse. If meridional circulation is weak, these latitudes would also experience the largest decrease in haze deposition.

The atmosphere resulting from the southern zonal band model becomes local between aphelion and northern winter solstice, but only for the lowest thermal inertias. At this point, the sublimation winds are equal in magnitude to the atmosphere's sound speed, and thus there will be large pressure variations across the surface Trafton and Stern (1983). As a result, the atmosphere becomes patchy and Io-like, extending only over the warmest patches of the surface. Any haze deposition would be restricted to these patches, which could build up surface contrasts. It could also reinforce existing contrasts. All else being equal, the darkest N_2 surfaces will be the warmest and could maintain an atmosphere above them. If the deposition of haze particles darkens the surface further, it would create a positive feedback that enhances existing surface contrasts. Conversely, a local atmosphere could shield the underlying surface from UV light, preventing ice-phase photolysis. Whether this would lead to positive or negative feedback depends on the relative albedo of the gas-phase and ice-phase photolysis products, and their rates of production.

A complication we have not considered here is a time-variable CH_4 mixing ratio in the atmosphere. The pressures we investigate here as being relevant to haze production (0.5 μbar haze aggregation limit, 0.06 μbar local atmosphere limit, and the 10^{-3} to 10^{-4} μbar atmospheric transparency limit) are determined from the atmospheric structure as observed in 2015 by New Horizons. Over time however, the mixing ratio of CH_4 could vary, changing the altitude at which the photochemical reactions producing the haze occur. For example, if the mixing ratio was about 10^{-3} times less than it is currently, the atmospheric transparency limit would be 10^3 times higher, at about 1 μbar, and many of our cases would interrupt haze. A variable CH_4 mixing ratio would also have implications for haze chemistry, changing the color and composition, as well as the production rate.

Grundy et al. (2018) and Bertrand et al. (2019b) describe other methods that could explain the observed surface heterogeneity, which we briefly summarize here. One mechanism could be differing thermal processing of the haze particles as they settle through the atmosphere, perhaps due to latitudinal or seasonal changes in the amount or type of hydrocarbons available to stick onto the haze monomers. If the haze particles are not all uniform but instead follow a distribution of characteristics such as size or albedo, then different parts of the distribution could respond differently in various surface environments. Another possible mechanism is cyclical burial and exhuming of haze particles, where the different surface appearances could represent freshly fallen hazes versus exhumed, previously buried haze particles. Over SP, katabatic winds blowing downslope could concentrate haze particles on the ice sheet, counteracting the sublimation winds' tendency to blow haze particles off of it (Bertrand et al., 2019b); aeolian processes could be important at the locations of other N_2 deposits as well.

5. Conclusions

Table 2 summarizes the results for each of the four N_2 distributions we investigate here, for Pluto's current orbit and configurations experienced over the past 10 My. 'Possible' indicates that a particular model predicts pressures for 1 or 2 of the test cases indicative of an atmosphere with the given characteristic (non-aggregating, local or UV transparent) for some portion of the orbit, while 'probable' indicates that 3 or more of the test cases predicted atmospheres with that characteristic. For the reference model, which has a bare southern hemisphere, haze production is not predicted to be interrupted at all, and the atmosphere will not collapse, neither in the current orbit nor over the past 10 My. Southern N_2 in some form is required to produce pressures below any of the haze-disruption pressures we considered. We investigated two example southern N_2 distributions: a south polar cap extending from the pole to 60°S with a fractional abundance of 20% and a southern zonal band between 35°S and 55°S, also with a fractional abundance of 20%. Other southern distributions are of course possible, but we chose these two to be representative of some of the possibilities. Atmospheric

		Non-Aggregating	Local	UV-Transparent
		<0.5 μbar	<0.06 μbar	$<10^{-3}$ to $<10^{-4}\mu$bar
Reference Model	Current	-	-	-
	Superseasons	-	-	-
Sputnik Planitia - Only	Current	possible	-	-
	Superseasons	possible	possible	-
South Polar Cap	Current	-	-	-
	Superseasons	possible	-	-
Southern Zonal Band	Current	probable	possible	-
	Superseasons	probable	possible	-

Table 2: Summary of the results for each of the spatial N_2 distributions we investigate. 'Possible' indicates that a particular model predicts pressures for 1 or 2 of the test cases indicative of an atmosphere with the given characteristic (non-aggregating, local or UV transparent) for some portion of the orbit, while 'probable' indicates that 3 or more of the test cases predicted atmospheres with that characteristic. Blank spaces indicate that the model-predicted pressure remain above that particular limit throughout the entire orbit. In the case of the superseasonal behavior, a blank indicates that the model-predicted pressures remain above the haze-disruption pressure for the entire 10 My we investigated.

collapse, when the pressure becomes too low to support a global atmosphere, only occurs in our southern zonal band model, and only for low thermal inertias (<200 tiu).

In general, the N_2 ices on the surface collectively re-radiate the insolation absorbed by only the illuminated ices. If more ice coverage is added to the southern hemisphere, currently in polar night, then these unilluminated ices will not absorb solar energy, but they will emit energy. Thus, the presence of obscured southern N_2 ices can lower the minimum pressure experienced over an orbit. However, in order to satisfy the constraints (doubling of the surface pressure since 1988 and an 11.5 μbar pressure in 2015), we found that N_2 distributions including southern N_2 required much lower thermal inertias.

The area of the southern hemisphere that is obscured in polar night won't decrease until after solstice occurs in 2029, and the entire southern hemisphere won't be visible until equinox occurs 100 years after that. The southern hemisphere could be thermally mapped when it is in polar night, providing a means to determine the spatial distribution of N_2 in the near future rather than a century from now. Our model predicts that there can only be small perennial southern deposits, since we were unable to match observable constraints for southern zonal bands or south polar caps with fractional abundances above 20%.

The most recent analysis of ground-based stellar occultations report a monotonic increase in Pluto's pressure between 1988 and 2016 (Meza et al., 2019). All of our models predict a turnover in the pressure by the 2030s, when the surface pressure will begin to decrease as Pluto moves toward aphelion and the subsolar latitude retreats to the southern hemisphere. However, the date of the turnover and the speed of the decline in pressure varies between distribution and chosen parameters in our model. Observations of the atmosphere pressure in the next few decades will thus be crucial for determining which N_2 distributions and which (A,Γ,ϵ) triplets best represent Pluto.

6. Acknowledgments

This work was supported in part by NASA ROSES SSW grant NNX15AH35G and by NASA's New Horizons mission to the Pluto system. The authors would also like to thank Tanguy Bertrand for illuminating discussions and feedback, as well as James Keane, Amanda Sickafoose, and Anja Genade for reviewing early versions of the appendix.

Appendix A. Approximating Temperatures with VT3D

Temperature from Analytic Approximation

Volatile Transport 3D (VT3D) uses an analytic approximation of the temperature evolution as an initial solution for the more accurate numerical solution. On its own, the analytic solution is often a good approximation and it is computationally more expedient. This appendix explains how to use the analytic approximation to calculate surface pressures over a period of one Pluto orbit, using the reference model as described in the paper.

The diurnally- and spatially-averaged incident insolation $S(t)$ can be represented using an analytic Fourier approximation:

$$S_0 = \frac{1}{P}\int_0^P S(t)dt \tag{A.1}$$

$$S_m = \frac{2}{P}\int_0^P S(t)e^{-im\omega t}dt \qquad m > 0 \tag{A.2}$$

where P is the period of the solar forcing (in this case, one Pluto year) and ω is the corresponding frequency. m is an integer corresponding to the mth Fourier term. For the reference model insolation, the first 11 Fourier terms are provided in Table A.3. These terms are for the diurnally- and spatially-averaged insolation onto the N_2-covered regions. The diurnally-averaged incident insolation as a function of latitude λ can be calculated via:

$$\overline{S(\lambda, t)} = \frac{\sin\lambda \sin\lambda_0 h_{max} + \cos\lambda\cos\lambda_0 \sin h_{max}}{\pi}\frac{L_{sun}}{4\pi r^2} \tag{A.3}$$

where λ_0 is the subsolar latitude, $L_{sun} = 3.828 \text{ x } 10^{26}$ W, and r is the heliocentric distance, in meters. The maximum illuminated hour angle at that latitude, h_{max}, can be found using: $\cos h_{max} = max(1, min(-\tan\lambda\tan\lambda_0, 1))$.

The time variable, t, represent time within in one Pluto year, and timesteps must be larger than one Pluto day (we used $\Delta t = 2$ Earth years). To spatially-average over the N_2-covered regions, we calculate:

$$S(t) = \frac{\int_{N_2} \overline{S(\lambda, t)} \Omega d\Omega}{\int_{N_2} \Omega d\Omega} \tag{A.4}$$

where Ω is the solid angle area of a patch on the surface covered by N_2 and the integral is performed over all patches.

m	S_m $[W/m^2]$
0	0.220561
1	0.115454 - 0.136762i
2	0.043688 - 0.068281i
3	0.015757 - 0.029367i
4	0.007107 - 0.011570i
5	0.003849 - 0.004378i
6	0.002244 - 0.001651i
7	0.001404 - 0.000616i
8	0.000920 - 0.000234i
9	0.000615 - 0.000097i
10	0.000408 - 0.000062i

Table A.3: Fourier terms for the incident insolation for the reference model described in this paper.

These insolation terms can be converted into temperatures using the following equation:

$$T(\zeta, t) = -\frac{F\zeta}{\Gamma\sqrt{\omega}} + T_0 + Re\left[\sum_{m=1}^{M} T_m e^{im\omega t} e^{\sqrt{im}\zeta}\right] \tag{A.5}$$

T_0 is the average temperature assuming thermal emission balances solar insolation and internal heat flux, F: $T_0 = ([(1-A)S_0 + F]/\epsilon\sigma)^{1/4}$. $\zeta = z/Z$ is the unitless depth of the layer, scaled by the skin depth, $Z = \sqrt{k/(\rho c \omega)}$. For N_2 ice, we use density $\rho = 1000$ kg/m^3, specific heat c = 1300 J/(kg K), and calculate the heat conductivity k based on the selected thermal inertia value ($\Gamma = \sqrt{k\rho c}$). For surface temperatures, the depth z = 0.

Each temperature Fourier coefficient is given by:

$$T_m = \frac{(1-A)S_m}{\Phi_E(T_0)} \frac{4}{4 + \sqrt{im}\Theta_S(T_0) + im\Theta_A(T_0) \qquad m > 0} \tag{A.6}$$

where Φ_E is the derivative of the thermal emission with respect to temperature:

$$\Phi_E(T_0) = 4\epsilon\sigma T_0^3 \tag{A.7}$$

where the Stefan-Boltzmann constant $\sigma = 5.67$ x 10^{-8} W/m^2. The dimensionless thermal parameters Θ_S (buffering of volatile temperature due to thermal conduction to neighboring layers) and Θ_A (buffering due to latent heat of sublimation) are defined as:

$$\Theta_S(T_0) = \frac{\sqrt{\omega}\Gamma}{\Phi_E(T_0)/4} \tag{A.8}$$

$$\Theta_A(T_0) = \frac{\omega \frac{L_s}{f_v g} \frac{dp_s}{dT_V}\Big|_{T_0}}{\Phi_E(T_0)/4} \tag{A.9}$$

where L_s is the latent heat of sublimation for N_2: approximately 2.7 x 10^5 J/kg for α-phase (below 35.6 K) and 2.4 x 10^5 J/kg for β-phase (above 35.6 K). The surface gravity g is 0.62 m/s^2. The fraction of the surface covered by nitrogen ice, using our reference map, f_v, is 0.102. dp_s/dT_V is the derivative of the vapor pressure with respect to the volatile temperature, evaluated at T_0:

$$\left.\frac{dp_s}{dT_V}\right|_{T_0} = \frac{L_s m_V p_s(T_0)}{k_B T_0^2} \qquad \text{(A.10)}$$

where m_v is the molecular mass of N_2, $p_s(T_0)$ is the equilibrium vapor pressure above solid N_2 at temperature T_0, and k_B is the Boltzmann constant.

Selecting A, Γ, and ϵ

As described in this paper, VT3D has three free parameters that describe the nitrogen frost: the Bond albedo, A, the thermal inertia, Γ (in units of "tiu", J m^{-2} K^{-1} $s^{-1/2}$), and the emissivity, ϵ. We select values for A and Γ, and then choose a corresponding value for ϵ such that the pressure predicted by the model at the time of the New Horizons flyby is 11.5 μbar. It the paper, we iteratively calculate pressures with different emissivities until we find a solution that predicts the correct pressure in 2015. Here, we present a polynomial fit to the relationship this process derived. The coefficients k_i (which are each a function of A) in Table A.4 can be used along with the equation below to calculate the emissivity needed for the chosen albedo and thermal inertia value. The relationship predicts the necessary emissivity to within 2% of the correct value for most A and Γ values. Once the emissivity value for the chosen A and Γ has been calculated, Equation A.5 can be used to calculate the temperature at every point t within Pluto's orbit.

$$\epsilon(A,\Gamma) = k_0(A) + k_1(A)\Gamma + k_2(A)\Gamma^2 + k_3(A)\Gamma^3 + k_4(A)\Gamma^4 \qquad \text{(A.11)}$$

Albedo	$\mathbf{k}_0$	$\mathbf{k}_1$	$\mathbf{k}_2$	$\mathbf{k}_3$	$\mathbf{k}_4$
0.500	2.378e+00	-2.141e-03	1.760e-06	-7.190e-10	1.150e-13
0.525	2.254e+00	-2.116e-03	1.804e-06	-7.581e-10	1.240e-13
0.550	2.128e+00	-2.081e-03	1.835e-06	-7.910e-10	1.319e-13
0.575	2.001e+00	-2.033e-03	1.851e-06	-8.167e-10	1.385e-13
0.600	1.872e+00	-1.974e-03	1.855e-06	-8.378e-10	1.447e-13
0.625	1.741e+00	-1.901e-03	1.840e-06	-8.488e-10	1.488e-13
0.650	1.607e+00	-1.808e-03	1.795e-06	-8.429e-10	1.496e-13
0.675	1.473e+00	-1.700e-03	1.731e-06	-8.268e-10	1.484e-13
0.700	1.336e+00	-1.575e-03	1.642e-06	-7.961e-10	1.444e-13
0.725	1.198e+00	-1.430e-03	1.521e-06	-7.467e-10	1.365e-13
0.750	1.060e+00	-1.272e-03	1.378e-06	-6.843e-10	1.260e-13
0.775	9.222e-01	-1.097e-03	1.206e-06	-6.034e-10	1.115e-13
0.800	7.870e-01	-9.185e-04	1.026e-06	-5.191e-10	9.667e-14
0.825	6.551e-01	-7.360e-04	8.343e-07	-4.262e-10	7.994e-14
0.850	5.288e-01	-5.562e-04	6.371e-07	-3.277e-10	6.177e-14
0.875	4.102e-01	-3.872e-04	4.459e-07	-2.302e-10	4.352e-14
0.900	3.022e-01	-2.428e-04	2.810e-07	-1.458e-10	2.766e-14
0.925	2.064e-01	-1.265e-04	1.449e-07	-7.470e-11	1.412e-14
0.950	1.247e-01	-4.950e-05	5.585e-08	-2.858e-11	5.377e-15
0.975	5.706e-02	-1.293e-05	1.536e-08	-8.019e-12	1.512e-15

Table A.4: Coefficients (as a function of albedo) needed to calculate the emissivity.

References

Bertrand, T., Forget, F., 2016. Observed glacier and volatile distribution on Pluto from atmosphere-topography processes. Nature 540, 86–89. doi:10.1038/nature19337.

Bertrand, T., Forget, F., 2017. 3D modeling of organic haze in Pluto's atmosphere. ??jnlIcarus 287, 72–86. doi:10.1016/j.icarus.2017.01.016, arXiv:1702.03783.

Bertrand, T., Forget, F., Umurhan, O.M., Grundy, W.M., Schmitt, B., Protopapa, S., Zangari, A.M., White, O.L., Schenk, P.M., Singer, K.N., 2018. The nitrogen cycles on Pluto over seasonal and astronomical timescales. Icarus 309, 277–296. doi:10.1016/j.icarus.2018.03.012, arXiv:1804.02434.

Bertrand, T., Forget, F., Umurhan, O.M., Moore, J.M., Young, L.A., Protopapa, S., Grundy, W.M., Schmitt, B., Dhingra, R.D., Binzel, R.P., Earle, A.M., Cruikshank, D.P., Stern, S.A., Weaver, H.A., Ennico, K., Olkin, C.B., New Horizons Science Team, 2019a. The CH_4 cycles on Pluto over seasonal and astronomical timescales. Icarus 329, 148–165. doi:10.1016/j.icarus.2019.02.007, arXiv:1903.02096.

Bertrand, T., Forget, F., White, O., Schmitt, B., 2019b. Pluto's beating heart regulates the atmospheric circulation: results from high resolution and multi-year numerical climate simulations. Journal of Geophysical Research Submitted.

Buratti, B.J., Hofgartner, J.D., Hicks, M.D., Weaver, H.A., Stern, S.A., Momary, T., Mosher, J.A., Beyer, R.A., Verbiscer, A.J., Zangari, A.M., Young, L.A., Lisse, C.M., Singer, K., Cheng, A., Grundy, W., Ennico, K., Olkin, C.B., 2017. Global albedos of Pluto and Charon from LORRI New Horizons observations. ??jnlIcarus 287, 207–217. doi:10.1016/j.icarus.2016.11.012, arXiv:1604.06129.

Cheng, A.F., Summers, M.E., Gladstone, G.R., Strobel, D.F., Young, L.A., Lavvas, P., Kammer, J.A., Lisse, C.M., Parker, A.H., Young, E.F., Stern, S.A., Weaver, H.A., Olkin, C.B., Ennico, K., 2017. Haze in Pluto's atmosphere. Icarus 290, 112–133. doi:10.1016/j.icarus.2017.02.024, arXiv:1702.07771.

Earle, A.M., Binzel, R.P., Young, L.A., Stern, S.A., Ennico, K., Grundy, W., Olkin, C.B., Weaver, H.A., New Horizons Geology and Geophysics Imaging Team, 2017. Long-term surface temperature modeling of Pluto. Icarus 287, 37–46. doi:10.1016/j.icarus.2016.09.036.

Earle, A.M., Binzel, R.P., Young, L.A., Stern, S.A., Ennico, K., Grundy, W., Olkin, C.B., Weaver, H.A., New Horizons Surface Composition Theme, 2018. Albedo matters: Understanding runaway albedo variations on Pluto. Icarus 303, 1–9. doi:10.1016/j.icarus.2017.12.015.

Elliot, J.L., Dunham, E.W., Bosh, A.S., Slivan, S.M., Young, L.A., Wasserman, L.H., Millis, R.L., 1989. Pluto's atmosphere. Icarus 77, 148–170. doi:10.1016/0019-1035(89)90014-6.

Elliot, J.L., Person, M.J., Qu, S., 2003. Analysis of Stellar Occultation Data. II. Inversion, with Application to Pluto and Triton. Astronomical Journal 126, 1041–1079. doi:10.1086/375546.

Fray, N., Schmitt, B., 2009. Sublimation of ices of astrophysical interest: A bibliographic review. Planetary and Space Science 57, 2053–2080. doi:10.1016/j.pss.2009.09.011.

Grundy, W.M., Bertrand, T., Binzel, R.P., Buie, M.W., Buratti, B.J., Cheng, A.F., Cook, J.C., Cruikshank, D.P., Devins, S.L., Dalle Ore, C.M., Earle, A.M., Ennico, K., Forget, F., Gao, P., Gladstone, G.R., Howett, C.J.A., Jennings, D.E., Kammer, J.A., Lauer, T.R., Linscott, I.R., Lisse, C.M., Lunsford, A.W., McKinnon, W.B., Olkin, C.B., Parker, A.H., Protopapa, S., Quirico, E., Reuter, D.C., Schmitt, B., Singer, K.N., Spencer, J.A., Stern, S.A., Strobel, D.F., Summers, M.E., Weaver, H.A., Weigle, G.E., Wong, M.L., Young, E.F., Young, L.A., Zhang, X., 2018. Pluto's haze as a surface material. Icarus 314, 232–245. doi:10.1016/j.icarus.2018.05.019, arXiv:1903.03728.

Grundy, W.M., Fink, U., 1996. Synoptic CCD Spectrophotometry of Pluto Over the Past 15 Years. Icarus 124, 329–343. doi:10.1006/icar.1996.0208.

Hansen, C.J., Paige, D.A., 1996. Seasonal Nitrogen Cycles on Pluto. Icarus 120, 247–265. doi:10.1006/icar.1996.0049.

Hansen, C.J., Paige, D.A., Young, L.A., 2015. Pluto's climate modeled with new observational constraints. ??jnlIcarus 246, 183–191. doi:10.1016/j.icarus.2014.03.014.

Hapke, B., 1993. Theory of reflectance and emittance spectroscopy.

Hinson, D.P., Linscott, I.R., Young, L.A., Tyler, G.L., Stern, S.A., Beyer, R.A., Bird, M.K., Ennico, K., Gladstone, G.R., Olkin, C.B., Pätzold, M., Schenk, P.M., Strobel, D.F., Summers, M.E., Weaver, H.A., Woods, W.W., 2017. Radio occultation measurements of Pluto's neutral atmosphere with New Horizons. Icarus 290, 96–111. doi:10.1016/j.icarus.2017.02.031.

Howard, A.D., Moore, J.M., Umurhan, O.M., White, O.L., Anderson, R.S., McKinnon, W.B., Spencer, J.R., Schenk, P.M., Beyer, R.A., Stern, S.A., Ennico, K., Olkin, C.B., Weaver, H.A., Young, L.A., New Horizons Science Team, 2017. Present and past glaciation on Pluto. Icarus 287, 287–300. doi:10.1016/j.icarus.2016.07.006.

Hubbard, W.B., Hunten, D.M., Dieters, S.W., Hill, K.M., Watson, R.D., 1988. Occultation evidence for an atmosphere on Pluto. Nature 336, 452–454. doi:10.1038/336452a0.

Lellouch, E., Santos-Sanz, P., Lacerda, P., Mommert, M., Duffard, R., Ortiz, J.L., Müller, T.G., Fornasier, S., Stansberry, J., Kiss, C., 2013. "TNOs are Cool": A survey of the trans-Neptunian region. IX. Thermal properties of Kuiper belt objects and Centaurs from combined Herschel and Spitzer observations. Astronomy and Astrophysics 557, A60. doi:10.1051/0004-6361/201322047.

Lewis, B.L., Stansberry, J.A., Holler, B.J., Grundy, W.M., Schmitt, B., Protopapa, S., Lisse, C., Stern, S.A., Young, L.A., Weaver, H.A., Olkin, C., Ennico, K., the New Horizons Science Team, 2019. Distribution and Energy Balance of Pluto's Nitrogen Ice, as seen by New Horizons in 2015. Icarus Submitted.

McKinnon, W.B., Nimmo, F., Wong, T., Schenk, P.M., White, O.L., Roberts, J.H., Moore, J.M., Spencer, J.R., Howard, A.D., Umurhan, O.M., Stern, S.A., Weaver, H.A., Olkin, C.B., Young, L.A., Smith, K.E., Beyer, R., Buie, M., Buratti, B., Cheng, A., Cruikshank, D., Dalle Ore, C., Gladstone, R., Grundy, W., Lauer, T., Linscott, I., Parker, J., Porter, S., Reitsema, H., Reuter, D., Robbins, S., Showalter, M., Singer, K., Strobel, D., Summers, M., Tyler, L., Banks, M., Barnouin, O., Bray, V., Carcich, B., Chaikin, A., Chavez, C., Conrad, C., Hamilton, D., Howett, C., Hofgartner, J., Kammer, J., Lisse, C., Marcotte, A., Parker, A., Retherford, K., Saina, M., Runyon, K., Schindhelm, E., Stansberry, J., Steffl, A., Stryk, T., Throop, H., Tsang, C., Verbiscer, A., Winters, H., Zangari, A., New Horizons Geology, G., Team, I.T., 2016. Convection in a volatile nitrogen-ice-rich layer drives Pluto's geological vigour. 534, 82–85. doi:10.1038/nature18289, arXiv:1903.05571.

Meza, E., Sicardy, B., Assafin, M., Ortiz, J.L., Bertrand, T., Lellouch, E., Desmars, J., Forget, F., Bérard, D., Doressoundiram, A., Lecacheux, J., Oliveira, J.M., Roques, F., Widemann, T., Colas, F., Vachier, F., Renner, S., Leiva, R., Braga-Ribas, F., Benedetti-Rossi, G., Camargo, J.I.B., Dias-Oliveira, A., Morgado, B., Gomes-Júnior, A.R., Vieira-Martins, R., Behrend, R., Tirado, A.C., Duffard, R., Morales, N., Santos-Sanz, P., Jelínek, M., Cunniffe, R., Querel, R., Harnisch, M., Jansen, R., Pennell, A., Todd, S., Ivanov, V.D., Opitom, C., Gillon, M., Jehin, E., Manfroid, J., Pollock, J., Reichart, D.E., Haislip, J.B., Ivarsen, K.M., LaCluyze, A.P., Maury, A., Gil-Hutton, R., Dhillon, V., Littlefair, S., Marsh, T., Veillet, C., Bath, K.L., Beisker, W., Bode, H.J., Kretlow, M., Herald, D., Gault, D., Kerr, S., Pavlov, H., Faragó, O., Klös, O., Frappa, E., Lavayssière, M., Cole, A.A., Giles, A.B., Greenhill, J.G., Hill, K.M., Buie, M.W., Olkin, C.B., Young, E.F., Young, L.A., Wasserman, L.H., Devogèle, M., French, R.G., Bianco, F.B., Marchis, F., Brosch, N., Kaspi, S., Polishook, D., Manulis, I., Ait Moulay Larbi, M., Benkhaldoun, Z., Daassou, A., El Azhari, Y., Moulane, Y., Broughton, J., Milner, J., Dobosz, T., Bolt, G., Lade, B., Gilmore, A., Kilmartin, P., Allen, W.H., Graham, P.B., Loader, B., McKay, G., Talbot, J., Parker, S., Abe, L., Bendjoya, P., Rivet, J.P., Vernet, D., Di Fabrizio, L., Lorenzi, V., Magazzú, A., Molinari, E., Gazeas, K., Tzouganatos, L., Carbognani, A., Bonnoli, G., Marchini, A., Leto, G., Sanchez, R.Z., Mancini, L., Kattentidt, B., Dohrmann, M., Guhl, K., Rothe, W., Walzel, K., Wortmann, G., Eberle, A., Hampf, D., Ohlert, J., Krannich, G., Murawsky, G., Gährken, B., Gloistein, D., Alonso, S., Román, A., Communal, J.E., Jabet, F., deVisscher, S., Sérot, J., Janik, T., Moravec, Z., Machado, P., Selva, A., Perelló, C., Rovira, J., Conti, M., Papini, R., Salvaggio, F., Noschese, A., Tsamis, V., Tigani, K., Barroy, P., Irzyk, M., Neel, D., Godard, J.P., Lanoiselée, D., Sogorb, P., Vérilhac, D., Bretton, M., Signoret, F., Ciabattari, F., Naves, R., Boutet, M., De Queiroz, J., Lindner, P., Lindner, K., Enskonatus, P., Dangl, G., Tordai, T., Eichler, H., Hattenbach, J., Peterson, C., Molnar, L.A., Howell, R.R., 2019. Lower atmosphere and pressure evolution on Pluto from ground-based stellar occultations, 1988-2016. 625, A42. doi:10.1051/0004-6361/201834281, `arXiv:1903.02315`.

Moore, J.M., McKinnon, W.B., Spencer, J.R., Howard, A.D., Schenk, P.M., Beyer, R.A., Nimmo, F., Singer, K.N., Umurhan, O.M., White, O.L., Stern, S.A., Ennico, K., Olkin, C.B., Weaver, H.A., Young, L.A., Binzel, R.P., Buie, M.W., Buratti, B.J., Cheng, A.F., Cruikshank, D.P., Grundy, W.M., Linscott, I.R., Reitsema, H.J., Reuter, D.C., Showalter, M.R., Bray, V.J., Chavez, C.L., Howett, C.J.A., Lauer, T.R., Lisse, C.M., Parker, A.H., Porter, S.B., Robbins, S.J., Runyon, K., Stryk, T., Throop, H.B., Tsang, C.C.C., Verbiscer, A.J., Zangari, A.a.M., Chaikin, A.L., Wilhelms, D.E., Bagenal, F., Gladstone, G.R., Andert, T., Andrews, J., Banks, M., Bauer, B., Bauman, J., Barnouin, O.S., Bedini, P., Beisser, K., Bhaskaran, S., Birath, E., Bird, M., Bogan, D.J., Bowman, A., Brozovic, M., Bryan, C., Buckley, M.R., Bushman, S.S., Calloway, A., Carcich, B., Conard, S., Conrad, C.A., Cook, J.C., Custodio, O.S., Ore, C.M.D., Deboy, C., Dischner, Z.J.B., Dumont, P., Earle, A.M., Elliott, H.A., Ercol, J., Ernst, C.M., Finley, T., Flanigan, S.H., Fountain, G., Freeze, M.J., Greathouse, T., Green, J.L., Guo, Y., Hahn, M., Hamilton, D.P., Hamilton, S.A., Hanley, J., Harch, A., Hart, H.M., Hersman, C.B., Hill, A., Hill, M.E., Hinson, D.P., Holdridge, M.E., Horanyi, M., Jackman, C., Jacobson, R.A., Jennings, D.E., Kammer, J.A., Kang, H.K., Kaufmann, D.E., Kollmann, P., Krimigis, S.M., Kusnierkiewicz, D., Lee, J.E., Lindstrom, K.L., Lunsford, A.W., Mallder, V.A., Martin, N., McComas, D.J., McNutt, R.L., Mehoke, D., Mehoke, T., Melin, E.D., Mutchler, M., Nelson, D., Nunez, J.I., Ocampo, A., Owen, W.M., Paetzold, M., Page, B., Parker, J.W., Pelletier, F., Peterson, J., Pinkine, N., Piquette, M., Protopapa, S., Redfern, J., Roberts, J.H., Rogers, G., Rose, D., Retherford, K.D., Ryschkewitsch, M.G., Schindhelm, E., Sepan, B., Soluri, M., Stanbridge, D., Steffl, A.J., Strobel, D.F., Summers, M.E., Szalay, J.R., Tapley, M., Taylor, A., Taylor, H., Tyler, G.L., Versteeg, M.H., Vincent, M., Webbert, R., Weidner, S., Weigle, G.E., Whittenburg, K., Williams, B.G., Williams, K., Williams, S., Woods, W.W., Zirnstein, E., 2016. The geology of Pluto and Charon through the eyes of New Horizons. Science 351, 1284–1293. doi:10.1126/science.aad7055, arXiv:1604.05702.

Olkin, C.B., Spencer, J.R., Grundy, W.M., Parker, A.H., Beyer, R.A., Schenk, P.M., Howett, C.J.A., Stern, S.A., Reuter, D.C., Weaver, H.A., Young, L.A., Ennico, K., Binzel, R.P., Buie, M.W., Cook, J.C., Cruikshank, D.P., Dalle Ore, C.M., Earle, A.M., Jennings, D.E., Singer, K.N., Linscott, I.E., Lunsford, A.W., Protopapa, S., Schmitt, B., Weigle, E., the New Horizons Science Team, 2017. The Global Color of Pluto from New Horizons. Astronomical Journal 154, 258. doi:10.3847/1538-3881/aa965b.

Owen, T.C., Roush, T.L., Cruikshank, D.P., Elliot, J.L., Young, L.A., de Bergh, C., Schmitt, B., Geballe, T.R., Brown, R.H., Bartholomew, M.J., 1993. Surface Ices and the Atmospheric Composition of Pluto. Science 261, 745–748. doi:10.1126/science.261.5122.745.

Protopapa, S., Grundy, W.M., Reuter, D.C., Hamilton, D.P., Dalle Ore, C.M., Cook, J.C., Cruikshank, D.P., Schmitt, B., Philippe, S., Quirico, E., Binzel, R.P., Earle, A.M., Ennico, K., Howett, C.J.A., Lunsford, A.W., Olkin, C.B., Parker, A., Singer, K.N., Stern, A., Verbiscer, A.J., Weaver, H.A., Young, L.A., New Horizons Science Team, 2017. Pluto's global surface composition through pixel-by-pixel Hapke modeling of New Horizons Ralph/LEISA data. Icarus 287, 218–228. doi:10.1016/j.icarus.2016.11.028, arXiv:1604.08468.

Schmitt, B., Philippe, S., Grundy, W.M., Reuter, D.C., Côte, R., Quirico, E., Protopapa, S., Young, L.A., Binzel, R.P., Cook, J.C., 2017. Physical state and distribution of materials at the surface of Pluto from New Horizons LEISA imaging spectrometer. Icarus 287, 229–260. doi:10.1016/j.icarus.2016.12.025.

Spencer, J.R., Moore, J.M., 1992. The influence of thermal inertia on temperatures and frost stability on Triton. Icarus 99, 261–272. doi:10.1016/0019-1035(92)90145-W.

Spencer, J.R., Stansberry, J.A., Trafton, L.M., Young, E.F., Binzel, R.P., Croft, S.K., 1997. Volatile Transport, Seasonal Cycles, and Atmospheric Dynamics on Pluto. p. 435.

Stansberry, J.A., Pisano, D.J., Yelle, R.V., 1996. The emissivity of volatile ices on Triton and Pluto. Planetary and Space Science 44, 945–955. doi:10.1016/0032-0633(96)00001-3.

Stern, S., Bagenal, F., Ennico, K., Gladstone, G., Grundy, W., McKinnon, W., Moore, J., Olkin, C., Spencer, J., Weaver, H., et al., 2015. The pluto system: Initial results from its exploration by new horizons. Science 350, aad1815.

Trafton, L., Stern, S.A., 1983. On the global distribution of Pluto's atmosphere. Astrophysical Journal 267, 872–881. doi:10.1086/160921.

White, O.L., Moore, J.M., McKinnon, W.B., Spencer, J.R., Howard, A.D., Schenk, P.M., Beyer, R.A., Nimmo, F., Singer, K.N., Umurhan, O.M., Stern, S.A., Ennico, K., Olkin, C.B., Weaver, H.A., Young, L.A., Cheng, A.F., Bertrand, T., Binzel, R.P., Earle, A.M., Grundy, W.M., Lauer, T.R., Protopapa, S., Robbins, S.J., Schmitt, B., New Horizons Science Team, 2017. Geological mapping of Sputnik Planitia on Pluto. Icarus 287, 261–286. doi:10.1016/j.icarus.2017.01.011.

Young, E.F., Binzel, R.P., 1993. Comparative Mapping of Pluto's Sub-Charon Hemisphere: Three Least Squares Models Based on Mutual Event Lightcurves. Icarus 102, 134–149. doi:10.1006/icar.1993.1038.

Young, L.A., 2012. Volatile transport on inhomogeneous surfaces: I - Analytic expressions, with application to Pluto's day. Icarus 221, 80–88. doi:10.1016/j.icarus.2012.06.032, `arXiv:1205.1382`.

Young, L.A., 2013. Pluto's Seasons: New Predictions for New Horizons. Astrophysical Journal Letters 766, L22. doi:10.1088/2041-8205/766/2/L22, `arXiv:1210.7778`.

Young, L.A., 2017. Volatile transport on inhomogeneous surfaces: II. Numerical calculations (VT3D). Icarus 284, 443–476. doi:10.1016/j.icarus.2016.07.021.